Dynamics and sources of last glacial aeolian deposition in southwest France derived from dune patterns, grain-size gradients and geochemistry, and reconstruction of efficient wind directions

Luca Sitzia, Pascal Bertran, Adriana Sima, Philippe Chery, Alain Queffelec, Denis-Didier Rousseau

Dynamics and sources of last glacial aeolian deposition in southwest France derived from dune pattern, grain-size gradients and geochemistry, and reconstruction of efficient wind directions.

Luca Sitzia[1], Pascal Bertran[2,3], Adriana Sima[4], Philippe Chery[5], Alain Queffelec[3], Denis-Didier Rousseau[6,7]

[1] Universidad de Tarapacá, Instituto de Alta Investigación, Laboratorio de Análisis e Investigaciones Arqueométricas, Antofagasta 1520, 1010069 Arica, Chile
[2] INRAP, 140 avenue Leclerc, 33130 Bègles, France
[3] PACEA, Université de Bordeaux – CNRS, bâtiment B18, allée Geoffroy-Saint-Hilaire, 33615 Pessac cedex, France
[4] Laboratoire de Météorologie Dynamique/IPSL, Sorbonne Universités, UPMC Université Paris 06, ENS, PSL Research University, École polytechnique, Université Paris Saclay, CNRS, Paris, France
[5] Bordeaux Sciences Agro, 1 cours du Général de Gaulle, CS 40201, 33175 Gradignan, France
[6] Laboratoire de Météorologie Dynamique/IPSL, Département de géosciences, ENS, PSL Research University, École Polytechnique, Université Paris Saclay, Sorbonne Universités, UPMC Université Paris 06, CNRS, Paris, France
[7] Lamont-Doherty Earth Observatory of Columbia University, Palisades, NY 10964, USA

Abstract

Dune pattern, grain-size gradients and geochemistry were used to investigate the sources and dynamics of aeolian deposition during the last glacial in southwest France. The coversands form widespread fields of low-amplitude ridges (zibars), whereas Younger Dryas parabolic dunes mainly concentrate in corridors and along rivers. Spatial modelling of grain-size gradients combined with geochemical analysis points to a genetic relationship between coversands and loess, the latter resulting primarily from dust produced by aeolian abrasion of the coversands. The alluvium of the Garonne river provided also significant amounts of dust at a more local scale. The geochemical composition of loess shows much lower scattering than that of coversands, due to stronger homogenisation during transport in the atmosphere. Overall, sandy loess and loess deposits decrease in thickness away from the coversands. Dune orientation and grain-size gradients suggest that the efficient winds blew respectively from the

W to the NW during the glacial, and the W-SW during the Younger Dryas. A comparison between the wind directions derived from the proxy data and those provided by palaeoclimatic simulations suggests a change of the main transport season. Ground surface conditions and their evolution throughout the year, i.e. the length of the season with snow and frozen or moist topsoil, and the seasonal distribution of wind speeds able to cause deflation are thought to have been the main factors that controlled the transport season in the study area.

Key words: coversand, loess, Last Glacial, dunes, grain-size modelling, geochemistry, wind direction, southwest France

1. **Introduction**

In the Aquitaine basin (Southwest France), Pleistocene coversands spread over a surface of approximately 12,000 km^2, and are bordered on their eastern and southern margins by a large loess belt. The stratigraphy of aeolian deposits has been the focus of recent studies and a large set of ^{14}C, ESR and OSL ages is available both for coversands and loess (Bertran et al., 2009, 2011; Hernandez et al., 2012; Sitzia et al., 2015). Mapping of aeolian deposits has also been the subject of many attempts. The conventional field approach allowed precise delineation of the coversands since the 60's (Enjalbert, 1960; Legigan, 1979), but the loess deposits were always omitted in the maps, and are still lacking on the current 1/50,000 geological map of France (*infoterre.brgm.fr*). Bertran et al. (2011) showed the potential of coupling field mapping and the use of soil databases designed for agricultural purposes, in which physico-chemical analyses of topsoil samples are listed. A first map of loess and transitional facies was produced using the online BDAT database (*www.gissol.fr*) where the sand, silt and clay content of topsoil samples are averaged at the scale of administrative units of an area of tens of square kilometers. Since then, the Land Use and Cover Area frame Statistical survey (LUCAS) database on topsoil properties in Europe has been made available and was used for further mapping of aeolian deposits (Bertran et al., 2016). The points which satisfy the grain-size criteria of coversands and loess were extracted from the rasters of predicted soil texture established by kriging of the LUCAS data by Balabio et al. (2016). These rasters have a resolution of 500 m. A comparison with previous maps showed a good fit in most of the tested areas in Europe (Bertran et al., 2016). Improvement of the French database (Donesol, *http://acklins.orleans.inra.fr/outil/donesol*) and access to raw data makes it now possible to investigate more in detail the aeolian deposits at a regional scale, since more refined information on grain-size composition and on loess thickness is available.

Pioneer mineralogical studies have been performed by Klingebiel (1966) and Legigan (1979). They have suggested that the sources of the coversands were mostly Mio-Pliocene alluvial and deltaic sands that crop out on the continental plateau. However, these studies remain crude, and the possible contribution of wind-blown particles derived from the alluvium fed by the surrounding ranges (Massif Central, Pyrenees) was hardly detectable using heavy mineral analyses alone. The provenance of the particles and the transport paths remain, therefore, to be documented in detail. Grain-size gradients (Lautridou, 1985; Ruegg, 1983; Liu, 1988), loess thickness (Frazee et al., 1970; Mason, 2001), and the mineralogical and chemical composition of the deposits (Muhs et al., 2008; Stevens et al., 2010; Rousseau et al. 2014) have proved to be efficient tools for reconstructing the transport paths at a regional scale and for identifying the main factors involved in deposition. Together with dune orientation, these data give insight into past atmospheric circulation and have been widely used for reconstructing wind directions during the Last Glacial in Europe (Poser, 1950; Maarleveld, 1960; Léger, 1990; Isarin et al., 1997; Zeeberg, 1998; Van Huissteden et al., 2001; Renssen et al., 2007).

The aim of this paper is to combined geomorphological, sedimentological and geochemical approaches to better understand the origin and dynamics of the aeolian deposition in southwest France. Then, the reconstructed wind regimes during the Last Glacial in the study area are compared with previous climatic simulations (Sima et al., 2009, 2013), in an attempt to identify the period of the year favourable to dust activity for different climate patterns.

2. Geological setting

Since the beginning of the Middle Pleistocene, the centre of the Aquitaine basin was quite similar to its current configuration and corresponded to a sand plain almost lacking relief and gently sloping toward the Atlantic Ocean. Such a context, unparalleled along the French coast, favoured the accumulation and preservation of aeolian deposits throughout the glacial phases of the Pleistocene (Bertran et al., 2011; Sitzia et al., 2015).

At the basin scale, the following geomorphological units have been distinguished (Fig.1B) : (1) ventifact pavements, present mainly in the northern part of the basin at the surface of the plateau alluvium on both sides of the Garonne River (Plateau Girondin and Blayais) ; (2) the coversands ("Sable des Landes Formation" *sensu* Sitzia et al., 2015), limited by the Garonne river to the east and the north, the Adour river to the south, and the Atlantic Ocean to the west; (3) a large loess belt mainly developed to the east and the south of the coversands.

Recent works allowed reappraisal of the regional chronostratigraphy of sand and loess deposits (Bertran *et al.*, 2009, 2011; Sitzia et al., 2015). Three main phases of coversand accumulation were identified throughout the Last Glacial (Sitzia et al. 2015): (1) Marine Isotopic Stage (MIS) 4-3 (64-32 ka), characterized by predominant wet sandsheet accumulation; (2) MIS 2 and the beginning of MIS 1 (Greenland Interstadial 1e) (25-14 ka), associated with the development of dry sandsheets and coincident with the maximum expansion of the Landes desert; (3) Younger Dryas (YD, Greenland Stadial 1), marked by the development of parabolic dune fields. Parabolic and dome dunes dating back to the 14th-19th centuries have also been documented and probably reflect local dune reactivation due to increased human impact on the vegetal cover during the Little Ice Age (Bertran et al., 2011).

Sitzia et al. (2015), through the analysis of the chronological data of near-surface coversands, revealed an uneven geographical distribution of the ages. They are dominantly Middle Pleistocene in the northernmost part, MIS 4-3 in the Plateau Girondin, and MIS 2 to YD in the Plateau Landais to the south. According to the authors, this pattern might have resulted from a deficit in sand in the north during the Last Glacial Maximum (LGM) since the emerged continental plateau was much wider (and as a consequence, the coastline was more distant) than in the south. Available ages for loess suggest that they accumulated mainly during the two last glacial periods (Bertran et al., 2011; Hernandez et al., 2012).

3. Modern wind regime.

Prevailing winds along the Atlantic coast of mid-latitude Western Europe are handled by two major pressure areas, the Azores High, located in the Atlantic Ocean between latitude 25 and 40°N, and the Icelandic Low, located between latitude 60 and 75°N. Seasonally, the position of these two pressure centres shifts and the wind regime changes. During the winter, dominant winds come from the southeast, whereas westerly to northwesterly winds are the most prominent during the summer (Fig. 2A). The map of mean wind speeds at 10 m available at the European Joint Research Centre (*http://agri4cast.jrc.ec.europa.eu/DataPortal*) shows the following (Fig.2B):

(1) The highest wind speeds are observed along the coast and in the Garonne estuary where channelling of the airflows leads to wind acceleration;

(2) Overall, the wind speeds decrease the further the altitude increases;

(3) The area with the lowest mean wind speed is located at the southern edge of the Pleistocene coversands.

4. Data and methods

4.1. Analysis of dune patterns

The pattern of the dune ridges has been analysed using (1) digitized black-and-white aerial photographs from the 1950 missions (1/25,000) of the French Institut Géographique National (IGN) and (2) IGN aerial colour photographs available on Google Earth. The main dune morphologies were described according to McKee (1979). To establish the crest direction we followed the approach proposed by Ewing et al. (2006). For barchanoid ridges, a line parallel to the general direction of the dune crest was used.

Most of the parabolic dunes have been mapped during the 1/50,000 geological survey of the Aquitaine basin by the French Bureau des Recherches Géologiques et Minières (BRGM) (Capdeville and Dubreuilh, 1994). The dune morphologies were described according to the terminology of Pye and Tsoar (2009), and the growth direction was measured using the bisector of the angle between the two arms of the dune.

Where available, the Digital Elevation Model (DEM) 5 m of the IGN (RGE Alti® 2.0, ©IGN 2014) made it possible the observation of the detailed morphology of the parabolic dunes. Since the small aeolian ridges remain difficult to identify from the DEM, a photogrammetric survey has been performed with a drone in 3 areas of 1 to 8 km^2, which provided more precise elevation data. The pixel resolution is 0.3 m.

4.2. Grain size, thickness and geochemistry of the aeolian deposits

The grain size and thickness dataset consists of (1) data collected in this work or previously published (Bertran et al., 2009, 2011; Dubreuilh, 1976; Thibault, 1970), and (2) data available from the Donesol database (INRA, 2011) for the Gironde, Landes, Dordogne and Lot-et-Garonne districts. The datasets were cleaned to select only the outcrops and the stratigraphical units of aeolian origin. The selected data were finally treated for the purpose of geostatistical analysis.

The samples for grain-size analysis were processed in the PACEA laboratory (Université de Bordeaux) using a Horiba LA-950 laser particle size analyser. The sample pre-treatment includes suspension in sodium hexametaphosphate (5 g/L) and hydrogen peroxide (35%) for 12 hours, and 60 seconds of ultrasonification in the analyser to achieve optimal dispersion. The Mie solution to Maxwell’s equations provided the basis for calculating the particle size as is recommended by the ISO committee (Jones, 2003; ISO, 2009), using a refractive index of 1,333 for water and 1.55i - 0.01i for the particles (see Supplementary Information 2). In the Donesol database, the grain-size limits are those used by the French pedologists (Duchaufour, 1997), i.e. 2000–200 µm (coarse sand), 200–50 µm (fine sand); 50–20 µm (coarse silt); 20–2 µm (fine silt); <2 µm (clay). The analyses used in the database have been done by wet sieving of the particles >50 µm and with the pipette method for the particles <50 µm. The results obtained with this method cannot be directly compared with those obtained with the laser particle size analyser (Konert and Vandenberghe, 1997; Buurman et al., 2001; Antoine et al., 2001). Here, after comparing 20 samples treated using both methods, the following limit classes have been chosen: <4.6 µm (clays), 4.6-26 µm (fine silt), 26-50 µm (coarse silt), >50 µm (sand). These limits are similar to those used by Antoine et al. (2003). Polymodal grain size distributions expressed in phi units have been deconvoluted in populations of particles characterized by a Gaussian distribution using the software Fityk 0.9.8 (Wojdyr, 2010) to identify precisely the main modes and to follow their spatial evolution.

The samples selected for the geochemical analysis (n=77) come from outcrops studied during this work or previously published (Bertran et al., 2009, 2011; Sitzia et al. 2015). The outcrops have been selected in order to characterize the main types of aeolian deposits and their potential sources: (1) Last Glacial coversands n=22) ; (2) YD parabolic dunes (n=13) ; (3)

loess from the Landes area (n=17) ; (4) loess from the Entre-Deux-Mers area (n=4) ; (5) recent alluvium of the Leyre (n=4), the Ciron (n=3), the Garonne (n=3) and the Adour (n=3) rivers; (6) Plio-Pleistocene plateau alluvial deposits (n=7). The samples from aeolian sands have been taken below the B horizon of the surface podzol. All the loess samples come from the argillic Bt horizon and were taken between 0.6 and 0.9 m deep. After removing the grains >2 mm, the sand fraction was separated from the component <63 µm by wet sieving and crushed. The sand and the fine fractions have been analyzed apart by Energy Dispersive X-Ray Fluorescence (ED-XRF) by the spectrometry division of Ametek (Elancourt, France). The measurements were made with a XEPOS instrument and do not allow quantification of elements lighter than aluminum. Quantification was based on fundamental parameters.

Some representative samples of aeolian deposits and possible sources have been studied by X-Ray Diffraction (XRD). As for ED-XRF, the sand and silt/clay fractions were studied separately. The analysis was carried out by the Institut de Chimie de la Matière Condensée in Bordeaux (ICMCB) using a PANalytical X'Pert diffractometer with a Bragg - Brentano theta – theta configuration. The measurements were made with a measuring time of 30 mn, between 8 and 80° and with a minimum step angle of 0.02°. Mineralogical identification was performed using the EVA software coupled with a JCPDS-ICDD PDF2 database.

The grain-size and the geochemical data are expressed as percentages; therefore, they have to be considered as compositional data (Aitchison, 1982). The analysis of compositional data by classic multivariate statistics provides inappropriate results (Aitchison, 1982). Aitchison (1986) proposed a robust solution to this problem, which used the logarithms of component ratios instead of the raw percentages. In this work, because of the nature of the data, we used non parametric replacement of the null values according to the method proposed by Martín-Fernández et al. (2003) for below-detection values. Here, all the compositional data were analysed using the CoDaPack software (Comas and Thió-Henestrosa, 2011).

For the purpose of geostatistical data analysis, a variographic analysis (Webster and Oliver, 2007) has been carried out with the VarioWin software (Pannatier, 1996). For compositional data, in agreement with Pawlowsky and Burger (1992), each variable was transformed before variographic analysis. Here, the Isometric Logratio Transformation has been applied (Egozcue et al., 2003). Finally, we used ordinary kriging (Webster and Oliver, 2007) for the interpolation through the geostatistical toolbox of ArcGis 9.3.

The models obtained have been tested by a double cross validation. In ArcGis, the value of a variable is estimated in each point of the space by kriging and this operation is repeated every time by removing one of the points for which the true value was originally known. Following this procedure, the software calculates the mean error (ME) and the mean square deviation ratio (MSDR). The mean error has to be close to 0, while the mean squared deviation ratio has be as close as possible to 1 (Webster and Oliver, 2007). The model validity has been also measured through an independent data set. The original database (grain size, thickness) selected for the geostatistical analysis has been split before the variographic analysis using the random selection spatial tool of ArcGis. We chose to randomly select 10% of the total number of samples. The remaining 90% have then been used for the variographic analysis and the calculation of the ME and MSDR statistics. Doing so, it was possible to plot the observed values (independent data set) against the estimated values and to calculate a linear regression between the two sets. Following Pawlowsky-Glahn and Olea (2004), the fitness of the regression for grain-size data was evaluated by calculating the standardized residual sum of squares (STRESS). The closer the value of the STRESS index to zero, the less is the difference between observed and estimated values, and thus the best is the tested modeling.

4.3. High-resolution glacial climate simulations

We dispose of two numerical palaeoclimatic simulations at high-resolution over the studied area that we can compare to our proxy data. The first simulation, designed for the Last Glacial Maximum (LGM), was used by Banks et al. (2009) for niche modelling. In this simulation, the orbital parameters and the atmospheric CO_2 concentration (Berger, 1978; Raynaud et al., 1993) were set to their values for 21 ka. The LGM ice-sheet configuration (height and extent) reconstructed by Peltier (2004, ICE-5G) was prescribed, and the land-sea mask was adjusted to a sea-level drop of about 120 m. The GLAMAP2000 reconstruction of the LGM sea-surface temperatures (SSTs) and sea-ice extent was imposed (Paul and Schäfer-Neth, 2003; Sarnthein et al., 2003). The second simulation is one of the numerical experiments used by Sima et al. (2009, 2013) to study the European climate (and dust) sensitivity to changes in North-Atlantic SSTs as those associated with the MIS 3 millennial-timescale variability. The orbital parameters and CO_2 concentration are set to 39 ka values, the ice-sheet configuration, also selected from the ICE-5G reconstructions, corresponds to a sea level about 60 m lower than today (i.e. half of the LGM value), and the land-sea mask is adapted to the sea-level drop. Because no reconstruction or modelling result was available at that time for MIS 3 sea-surface conditions, the GLAMAP2000 dataset was imposed in the base-line MIS 3 simulation. A cold and a warm perturbation were obtained by applying zonal anomalies of up to 2°C to the GLAMAP North-Atlantic SSTs in the latitudinal band between 30°N and 63°N. Considering the differences of North-Atlantic SSTs between the LGM and an average MIS 3 state suggested by experiments with an earth system model of intermediate complexity (Van Meerbeeck et al., 2009), here we use the warm perturbation (hereafter "MIS 3" simulation) to characterize the average MIS 3 conditions in the comparison with the LGM.

In both MIS 3 and LGM experiments, the modern vegetation cover was prescribed in most regions, following the PMIP recommendations (e.g. Braconnot, 2004). Thus, in the area of interest here, trees occupy 60-80% of every grid-point in the coversands (in yellow on Fig. 1B), and about 15- 40% elsewhere. The soil is bare all year long on 5-15% of the grid-points' surface, and the rest up to 100% of each grid-point is occupied by grass. This is a drawback because the LGM vegetation was much scarcer. The use of modern vegetation does not affect the simulated wind direction, but only the wind speed, which is strongly reduced due to overestimating the roughness length. As the wind speed is a key element in determining the season(s) when dust emissions occur, we also present sensitivity tests of this variable to more appropriate values of roughness length. Using prescribed present-day vegetation also leads to unrealistically overestimating its effect of protecting the ground from aeolian erosion. Thus, for the impact of the surface conditions on the dusty season, we will only be able to discuss soil moisture and snow cover.

The simulations were performed with the LMDZ atmospheric general circulation model (version 3.3), coupled with the SECHIBA land surface model (Krinner et al., 2005), on a stretched grid with resolution down to 60 km on Western Europe. For each simulation there are 21 years of run, one year of spin-up followed by 20 years for analyses.

5. Results

5.1. Dunes

5.1.1. Low amplitude dunes

Among the low amplitude dunes, four main morphological types have been identified from aerial photographs: transverse ridges, barchanoid ridges, isolated barchanoid ridges and dome dunes/sand patches. The ridges appear in cultivated areas as bright lineaments separated by darker interdune areas due to variations in soil organic and water content. Most of the ridge fields were observed in the Plateau Girondin area, where the groundwater table is close to the ground surface and the YD parabolic dunes are scarce. According to available chronological data, these ridges date back to MIS 4-3, or possibly to older phases of sand deposition in the northernmost area. The DEM provided by photogrammetry shows that the ridge pattern corresponds to regular to irregular low amplitude reliefs, 0.3 to 0.7 m high and 70 to 150 m in wavelength (Fig. 3). The reliefs are aligned along the bright lineaments visible in aerial photographs. In contrast, no significant ridge areas were found in aerial photographs to the south on the Plateau Landais where the MIS 2 coversands are thicker. Field survey, however, showed that ridges also were present there in small areas forming well-preserved linear reliefs approximately 1 m in height (Fig. 4). In cross-sections, all these dune-like forms are associated to a sandsheet facies; high-angle stratification is almost absent (Sitzia et al., 2015).

In the Plateau Girondin, the following observations can be made (Fig. 5): (1) the different types of ridge morphologies form homogeneous fields elongated parallel to the coast; (2) the dome dunes/sand patches are located on the margins of the barchanoid and transverse ridge fields; (3) the dune fields are replaced toward the east by an area characterized by thin sandsheet deposits almost lacking dune-like forms; (4) the distribution of the different types of morphologies seems to be mainly controlled by topography.

A total of 425 measurements of crest direction have been made from barchanoid and transverse ridges. The rose diagrams show that predominant crest directions are consistently N-S (i.e. the vector perpendicular to dune crests is W-E, Fig. 5A). Local departure from this direction was found to be mainly controlled by topography. This is particularly obvious in Figure 5C for the transverse ridges whose crest direction, roughly parallel to the contour lines, vary between N-S and NE-SW within a few kilometres.

5.1.2. Parabolic dunes

The parabolic dunes are 10 to 15 m high and exceptionally exceed 25 m (Dune de Cazalis, Legigan, 1979). The total number of digitized dunes is 2636. Following the typology proposed by Pye and Tsoar (2009), simple (hairpin, lunate), complex (hemicyclic, digitated, nested, rake-like, en-echelon) and compound (long-walled ridge with secondary transverse arms) forms were observed.

The parabolic dunes exhibit a non-random distribution over the landscape. They are mainly clustered around the rivers, and form corridors up to 80 km in length along shallow valleys oriented W-E and over the plateau (Fig. 6). The dune morphology changes according to topography. Along the Leyre and the Ciron valleys, as well as near the coast, the parabolic dunes are mostly simple; on the contrary, complex and compound forms are mainly observed in the corridors (Fig. 7A, C). Complex forms several kilometres in length have been observed in the main dune corridor (Fig. 7B).

A total of 394 measurements of dune orientation have been made. The rose diagrams reveal a systematic orientation towards the ENE and a low dispersion of the values (Fig. 6).

5.2. Grain-size gradients at the basin scale

In the Donesol grain-size database, 513 out of the 3683 sites, considered to be pure (i.e. non colluviated) aeolian deposits, were retained (Fig. 8). Among the selected sites, 462 were used in the geostatistical analysis and 51 for cross-validation. The results of cross-validation (see Supplementary Information) indicate that both the variographic analysis and the ordinary kriging were satisfactory. The interpolated maps of the content in coarse sand, fine sand, coarse silt and fine silt are shown in Figure 8. The following observations can be made: (1) every grain-size class shows a gradient oriented NW-SE; (2) the coarse fractions are mainly located in the north-western part of the basin and extend inland from Arcachon to the SE; (3) the Garonne and Adour valleys (and their tributaries) serve as limits for the coversands; the silty sand facies are restricted to a narrow strip on the left bank of the Garonne river, whereas they form a broader band on the right bank and in the southern part of the basin; (4) in the loess belt, the ratio coarse/fine silt varies only slightly in the study area. When increasing the number of grain-size classes, it can be observed that, both in the Entre-Deux-Mers area and in the southern part of the basin, the coarse silt maximum is located northwest of the fine silt maximum (Fig. 9). Comparison between these maps and that derived from the LUCAS database (Fig. 1) shows that loess have a more limited extent in the latter, where the mapped aeolian units have, therefore, to be considered as minimal.

The sand deposits extend up to the border of the Landes plateau and show a main mode ranging between 340 µm for the northernmost site (Retjons) and 270 µm for the southernmost one (Pujo-le-Plan) (Fig. 10B). In the Adour valley and its tributaries, the distribution is polymodal. From the north to the south, the main mode is first in medium sands (270 µm) and then decreases rapidly and gives way to a mode on silts (22 µm). In this area it can be noticed (1) a rapid decrease in the size of the sand particles (Fig. 10B); (2) a decrease in the contribution of the coarse modes in favour of the finer modes (Fig. 10C). Finally, south to the Adour valley, a mode around 17 µm becomes predominant (Fig. 11A). This mode decreases from 17 to 14 µm quite evenly as a function of the distance to the coversands. For all the sites located between the Adour valley and the Pyrenean foothills, significant amounts of clay are present. The mode, close to 3 µm, remains steady regardless of the distance to the coversands (Fig. 11A), whereas the total clay content slowly increases with distance (Fig. 10D).

In the northern part of the basin, the grain-size distributions show that (1) the sands of the Blayais area are relatively coarse (mode between 300 and 600 µm); (2) the silts of the Entre-Deux-Mers area have a mode between 30 and 34 µm; this is appreciably coarser than the mode of the loess deposits in the southern part of the basin; (3) the silt mode decreases significantly toward the SE. The most distant sample from the sources (Barbas) has a mode around 12 µm.

5.3 Thickness variability at the basin scale

According to Karnay et al. (2010), the coversands (Sable des Landes Formation) form a thin sheet, usually less than 2-3 m thick. Nevertheless, the underlying Castet Formation (Dubreuilh et al., 1995), which is now considered to be part of the Sable des Landes Formation (Sitzia et al., 2015) and reaches locally up to 40 m in thickness, was not considered by Karnay et al. (2010). As a whole, the coversand thickness decreases from the west to the east according to the distance to the coast and with altitude.

The loess data were partitioned in two sets, one for the north (n= 292), and the other for the south (n=434). The geostatistical analysis points out that (1) the ordinary kriging decreases systematically the standard deviation of the thickness around the mean; (2) the deviation between measured and estimated values is larger for the northern data set. The Anderson-

Darling test reveals that the deviation distribution fits a normal (Gaussian) distribution. For the southern loess, the accuracy of thickness estimation is 57.4 cm and the mean error is 81.8 cm. The most significant errors are due to extreme values. For the northern loess, the accuracy of estimation and the mean error cannot be evaluated because the deviation distribution does not follow a Gaussian function.

The interpolated maps show that the loess thickness decreases rapidly with increasing distance to the coversands, in a gradual way in the southern area, more steeply in the northern area (Fig. 12). The maximum loess thickness reaches 3.5 m in the south and 5 m in the north. Because of the uneven distribution of the selected Donesol data and the loose geographical coverage, the interpolated maps do not make it possible to identify if deposition preferentially occurred on particular slopes according to their orientation.

5.4. Geochemistry and potential sources

The distribution maps of elemental compositions (Fig. 13) and the scattergrams of the elements versus Si (Fig. 14) (mainly as quartz) point out the following:

(1) Zr, the principal component of zircon, and Ti, probably as oxides, are mainly concentrated in the fine fraction (silt, fine sand). Therefore, these elements are mostly abundant in loess and in the fine fraction of the coversands. In a Si-Ti diagram, the samples of aeolian deposits are aligned along a line with a negative slope (Fig. 14, line a), except for the fine fraction of some coversand samples. This strongly suggests that the most of the aeolian samples result from the size fractionation of a common source of intermediate composition between that of sand and that of fines (Fralick and Kronberg, 1997). The samples from the Adour and Garonne rivers also show a linear trend (line b), but plot on a different line from that of the aeolian deposits, which indicates different sources. On the contrary, the samples from the Leyre and the Ciron rivers, which drain both the coversands and old alluvial deposits, plot among the aeolian samples or between the Adour-Garonne and loess samples. Zr has a behaviour roughly similar to Ti. The loess composition appears to be homogeneous when compared with the whole data set. Such an observation is also valid for all the elements.

(2) Ca, as a component of carbonate or silicate minerals (feldspar, amphibole), is lacking in the aeolian sand fraction, whereas it has been found in small amount in the alluvial deposits. Ca has been detected as traces in the fine fraction of a few coversand samples where it is probably associated with Al in silicate minerals.

(3) K is present both in the aeolian sand fraction as part of silicate minerals (feldspar, muscovite) and in slightly larger amounts in the fine fraction (illite, mixed-layer illitic clay). Mean concentrations are significantly greater in the alluvial deposits. In the Si-K diagram, the K content of the aeolian sand fraction appears to be uncorrelated to Si and the samples are aligned on a horizontal line. On average, the sand fraction of loess is depleted in K in comparison with the coversands. The samples of fine fraction do not plot on the same line as the sands, but below it, suggesting a loss of K due to alteration and soil leaching (Fralick and Kronberg, 1997).

(4) On the Si-Al diagram (Fig. 14), the alignment of the aeolian samples along the same line suggests a partition of Al between sand and fines due to sedimentary sorting, with Al mainly concentrated in clays. High Al contents plotting above this line have been found only in the fine fraction of the coversands. Such enrichment in Al can be related to organic-mineral complexes in the B horizon of the surface podzol (Righi and De Coninck, 1974; Melkerud et al., 2000).

The principal component analysis ("compositional biplot", Aitchison and Greenacre, 2002) for the sand fraction (Fig. 15) explains 72.3% of the total variance. The first axis discriminates the group Ca+K+Rb+Sr from the group Fe+Ti+Zr. K and Rb are mainly related to K-silicates, mostly feldspar and micas (De Vos et al., 2006; Wedepohl, 1978). Sr has a size intermediate between K and Ca and can replace these two elements both in silicates and in carbonate minerals (De Vos *et al*., 2006). Because of the lack of carbonates in the studied samples, the group K+Rb+Sr reflects the pole of potassium silicates, while Ca corresponds to calcium silicates. Fe (+ Cr as a substitute) is present in silicate minerals and in oxides and hydroxides (De Vos *et al*., 2006). The group Fe, Ti and Zr thus represents the pole of oxides and the minerals resistant to alteration.

The position of the samples in the biplot allows making the following remarks: (1) the samples of aeolian sands (Landes, Blayais, parabolic_dunes), the old alluvial terraces of the

Garonne river (Plateau_alluvium), the recent alluvial deposits (Fz) of the Midou and Leyre rivers (which essentially drain the Sable des Landes Formation) are distributed between the barycentre of the biplot and the pole quartz + K-silicates; (2) the sand fraction of the southern loess (Loess_Landes) is associated with the pole of resistant minerals and oxides; (3) the recent alluvial deposits (Fz) of the Adour and Garonne rivers, which drain the Pyrenees, plot apart from the other samples, and are opposed to the pole quartz + resistant minerals; they include a high proportion of easily alterable Ca-minerals; (4) the sand fraction of the loess from the Entre-Deux-Mers area is located between the southern loess and the recent alluvial deposits.

The biplot for the fine fraction (Fig. 16), which takes into account a larger set of elements because of values above the detection limit, produces results substantially different from those for the sand fraction. It explains 63.7% of the total variance. Several poles can be distinguished. The first correspond to calcium-rich minerals (Ca); the second to resistant minerals, quartz and zircon (Si+Zr+Hf); the third to potassium silicates (K+Rb, and Ba, strongly adsorbed by soil clays, Reimann et al., 2014); and finally, the poles of Fe-oxides (Fe+Cr+As) and of Al-complexes (Al).

In this biplot, the loess samples appear more homogeneous and plot in the proximity of the pole oxides and K-silicates (probably dominated by clays). The loess composition partially covers that of coversands and is located apart of the recent alluvial deposits, which are close to the pole of Ca-minerals.

5.5. Results of climate simulations

Figure 17 shows the results of the LGM and MIS 3 simulations for wind direction and for the variables that constrain the period of the year when dust emissions can occur, i.e. daily maximum wind speed (more informative for dust mobilization than daily average), snow-free surface fraction, and dry soil depth. The annual cycle of these variables is constructed on daily data for winds, and on monthly data for surface conditions, averaged over 20 years of run for each climate state and over the domain between longitude 2°W-1°E and latitude 43°-45.5°N (delimited by the black rectangle in Fig. 1A and zoomed in Fig. 1B).

The annual cycle of wind direction (Fig. 17A, B) is similar in the two simulations and not much different from the present-day one (Fig. 2). In both cases, the winds blow from W-SW in winter, turn from W in springtime, then from W-NW in summer. A reverse evolution occurs from the summer to the winter, through westerly winds in autumn. The daily maximum wind speed, averaged over the domain and over 20 years of run (black curves in Fig. 17C, D), is highest in winter, lowest in summer, and springtime values are higher than autumn ones. The LGM daily maximum winds are generally stronger than for MIS 3, especially from mid-May to October. The differences are small, and the values themselves are relatively low, less than 7 $m.s^{-1}$. When looking at individual grid cells and individual days of the 7200-point time series (i.e., 20 years x 360 days/year of run on a 360-day calendar), the highest (winter) daily maximum winds in the MIS 3 run often exceed 12 $m.s^{-1}$, with peaks at about 16 $m.s^{-1}$, while in the LGM simulation the winter values are frequently above 16 $m.s^{-1}$, with extremes above 20 $m.s^{-1}$. The simulated winds are thus too weak considering the strong dust activity suggested by the field data. This is due to the high values of the roughness length (*z*0) calculated by the model on the basis of the present-day vegetation cover that was prescribed in both simulations. For comparison, z0 is about 37 cm on average on the studied domain, while values of 1 cm are associated in the model to bare soil. The vegetation was considerably scarcer than today for both LGM and average MIS 3 climates, so we recalculate and plot the daily maximum winds for two values of z0 more adapted to the investigated area and periods. The blue curves in Fig. 17C, D correspond to z0 = 1.5 cm, and the green ones to z0 = 4 cm. The first z0 value is the one that the model would calculate for a surface covered by about 50% of grass, and the rest of bare soil. The second one corresponds to a majority of grass, with less than 10% bare soil and less than 10% trees (that can be assimilated to shrubs, which are not represented in the model). With these lower z0, the averages of daily maximum wind increase considerably, they almost double for z0 = 1.5 cm. Looking at individual days and grid cells, even for the relatively less windy MIS 3 and the lower test value z0 = 4cm, the maximum daily values regularly exceed 25 $m.s^{-1}$ in winter, with a few peaks around 40 $m.s^{-1}$.

Park and In (2003) have statistically determined a wind-speed threshold of 7.5 $m.s^{-1}$ for dust mobilization in sandy areas from Asian deserts. If we consider this limit to also apply to the Landes coversands, the LGM average maximum winds practically never drop below it in the test with z0=1.5 cm, so that only the surface conditions would determine the dusty part of the year. For the MIS 3 run, the average daily maximum winds drop below the threshold in July for z0 = 1.5 cm, at mid-May for z0 = 4 cm respectively, and strengthen again in November in both tests. The tests with these z0 values can be interpreted in two ways. When comparing LGM to MIS 3, using the spatial averages of variables over the entire domain, the blue curve for the lower z0 (for about 50% grass and 50% bare soil) is more appropriate to characterize the LGM, and the green curve for the higher z0 (majority of grass, with some shrubs and bare soil) is more appropriate for a MIS 3 situation. For each of the LGM and MIS 3 simulations separately, the blue curve can be seen as representing the parts of the domain with scarce vegetation (mainly the coversands) and the green one, the more vegetated ones – mainly the loess areas, where part of the dust was trapped.

As a general evolution, the snow-free fraction of the surface and the depth of dry topsoil are low in the cold season and high in the warm one (Fig. 17E, F), the important question being to determine the interval when both variables are high enough to allow significant dust emissions.

In both simulations, most of the Landes surface is snow-free all year long. From October to February the depth of dry topsoil averaged over the domain is too small to allow a significant dust activity (a 5 mm threshold value was used in Sima et al. 2009). The dusty season could thus start in the beginning of March. At least for the LGM this is questionable, due to a warm winter bias causing an underestimation of both snow cover and soil moisture. Indeed, as mentioned in Banks et al. (2009), the simulated LGM climate over Western Europe is in agreement with pollen-based reconstructions (Wu et al., 2007) for summer and annual mean temperatures, and for mean annual precipitation, but winter cooling is underestimated by a few degrees. Thus, a comparison with the reconstructed directions for dust-efficient winds is needed to better constrain the beginning of the dusty season. Dust activity is strong until May or June, decreases to a minimum in July-August (it can even stop in more vegetated parts of the domain), and may briefly intensify again in September-October before ceasing from November to February due to unfavourable surface conditions (here soil moisture, in reality probably also snow).

In the MIS 3 simulation, the average dry soil depth becomes high enough to allow significant dust emissions in the beginning of March. Dust activity stops in May due to wind weakening, which actually may be accentuated by the seasonal development of vegetation, not captured in the simulation. According to the model, areas with scarce vegetation might continue to emit dust in the beginning of the summer. The simulated winds start to intensify again in autumn, but the increasing soil moisture plays against a restart of the emissions.

6. Discussion

6.1. Dunes

<u>Low amplitude ridges</u>

The ridges observed in the Gironde district, regardless of their morphology (transverse, barchanoid), are interpreted as zibars based on their low amplitude and the lack of slipface (Holm, 1960; Warren, 1972; Tsoar, 1978; Kocurek and Nielson, 1986; Nielson and Kocurek, 1986; Mountney and Russell, 2004). Zibars are often composed of coarse sand and the grain size is thought to be the main factor involved in preventing the development of a slipface (Bagnold, 1941; Cooke and Warren, 1973; Nielson and Kocurek, 1986).

The interpretation of the transverse and barchanoid ridges in the study area as zibars seems to be the most likely, even if they do not meet all the criteria mentioned above. Indeed, the zibars of the study area do not show a mode in coarse sands but in medium sands, similar to that found in parabolic dunes. With regards to dune morphology, we did not find in the literature zibar examples with a similar range of pattern (transverse, barchanoid, isolated ridges). Transverse and barchanoid ridges reflect unidirectional winds and point to sand transport perpendicular to the wind (Pye and Tsoar, 2009), in an environment almost devoid of vegetation.

The interpretation of the variations in dune pattern across the coversands is not straightforward, since the chronological data indicate that the ridge fields developed at different times: the barchanoid and transverse ridges in the Barp-Cestas area formed during MIS 4-3, whereas further north the barchanoid ridges date back to the Middle Pleistocene (Sitzia et al., 2015). Therefore, it remains unclear whether the morphological differences reflect changes in aeolian dynamics (especially in the availability of sand) during the same depositional phase or whether they testify to different periods of aeolian deposition. Nonetheless, it appears that topography, and particularly the slope gradient of the surface on which the ridges progressed, largely controlled their morphology.

Parabolic dunes

Parabolic dunes form in partially vegetated landscapes mainly under unidirectional winds, and are observed in all latitudes (Lancaster, 1995; Pye and Tsoar, 2009), along sandy coasts (Pye, 1982), but also inland (Sun and Muhs, 2007). They develop mainly from blowouts (Pye and Tsoar, 2009; Hesp, 2002; Barchyn and Hugenholtz, 2013). The morphology of parabolic dunes is controlled by the wind strength and direction, the sand supply and the nature of vegetated ground (Pye, 1982; Pye and Tsoar, 2009; Wolfe et al., 2008). The parabolic dunes gradually evolve into elongated forms. In some cases, the arms give rise to linear dunes when the sand supply is low.

According to available OSL and ^{14}C ages (Sitzia et al., 2015), the formation of the parabolic dunes in the Landes area took place mainly during the YD. The clusters of dunes along the valleys may suggest that the sand was partly supplied by the alluvium. However, the presence of dune corridors expanding over the plateau and of dunes located on the windward side of the valleys oriented N-S (e.g. Leyre, Ciron and Avance), testifies unambiguously that the local fluvial deposits were not the main sand sources. A coastal origin for the sand transported along the corridors parallel to the wind direction appears to be the most likely.

The development of dunes along the rivers resulted from the deceleration of the winds crossing the valleys. Wiggs et al. (2002) proposed the following conceptual model: (1) on the plateau area above the valley, erosion prevails and sediment accumulation is patchy; (2) on the windward side of the valley, the wind loses its carrying capacity and sediment tends to accumulate; (3) on the opposite side of the valley, the wind accelerates and the erosive potential increases; (4) on the plateau, the wind decelerates again over a short distance promoting sand deposition. This model correctly explains the dune distribution in the study area.

6.2. Loess sources and transport dynamics

The interpolated maps of sand and silt contents suggest a genetic relationship between the aeolian facies, as previously proposed by Bertran *et al.* (2011, 2016). The distribution of the contour lines shows a mean NW-SE gradient at the basin scale.

In the Landes and the Blayais areas, a gradual transition between coarse and fine sand deposits can be observed, which is not controlled by the nature of the substrate but reflects wind sorting and/or decreasing carrying capacity as suggested by the distribution of current mean wind speeds (Fig. 2). The sand-silt transition is mainly controlled by the topographic change that occurs between the plateau areas (Plateau Girondin, Plateau Landais, Blayais) and the main valleys (Garonne, Adour and Dordogne). Several authors have already outlined the role played by topography in the coversand-loess transition, among others Kasse (1997), Appelman (1956) and Mason et al. (1999). In the southern part of the basin, the transitional facies (silty sands and sandy silts) form a strip on the right bank of the Adour river, showing that deposition of the suspended particles was primarily triggered by the expansion of airflows above the valley. In the northern part of the basin, the transitional facies form a narrower belt on the left (windward) side of the Garonne valley (Fig. 8), in a context broadly comparable to the Adour area. In the estuary area to the north, the maps show an almost lack of fine-grained accumulation on both sides of the valley. The sand-loess transition shifts by approximately 40 km to the east. The abundant ventifacts found on the alluvial terraces point to a deflation-dominated area.

The geochemical analysis also strongly suggests a genetic relationship between coversand and loess. The sand fraction of the southern loess is depleted in K-silicates in comparison with the coversands and correlatively enriched in quartz and resistant minerals. The enrichment is especially obvious for Zr and Ti, which concentrate mainly in the fine fraction and tend broadly to increase as a function of the distance to the coversands. Such a preferential accumulation of Zr and Ti in loess deposits has been observed worldwide (Gallet et al., 1998; Scheib et al., 2014) and is interpreted as resulting mainly from grain-size sorting. The recent alluvial deposits of the Adour river, which are rich in Ca-minerals, did not contribute significantly to dust production, which derive mainly from the coversands. In the Entre-Deux-Mers area, the alluvium of the Garonne river provided higher amounts of dust, as suggested by the larger content of easily alterable minerals in the sand fraction of the loess and, to a lesser extent, in the fine fraction. Overall, loess appears to be much more homogeneous than coversand, whose composition is closer to the alluvial sources. We assume that this homogeneity results from the mixing in the atmosphere of the different dust sources (Gallet et al., 1998).

The maps of the thickness of aeolian deposits, which cumulate several sedimentary phases, provide complementary information. In the northern part of the basin, the thickest loess deposits are located close to the Garonne valley in the Entre-Deux-Mers area and show rapid thinning toward the east (Fig. 12A). In the southern area (Fig. 12B), the loess deposits are mainly located on the left bank of the Adour river and decrease in thickness more gradually toward both the south and the east. Distinct areas of thick loess accumulation are visible on the maps but can be, at least in part, an artefact due to kriging using a limited number of data. The observed pattern of loess thickness can be explained by the following factors:

(1) The distance to the dust sources. Close to the sources, the decrease in thickness of the deposits is initially very rapid because the coarser particles, which occupy a large volume, accumulate at short distances. Farther, the decrease is more gradual and due to lower concentration of suspended particles in the dust clouds (Simonson and Hutton, 1954; Waggoner and Bingham, 1961; Frazee et al., 1970). The observed pattern points clearly to the Sable des Landes Formation and the Blayais sands as the main sources of dust. The rivers (Dordogne, Lot) flowing from the Massif Central mountains did not provide significant amounts of dust, as suggested by the lack of variation in loess thickness around the valleys. A plausible explanation is that armouring developed quickly in the dominantly coarse-grained alluvial deposits during the Glacial, preventing significant dust entrainment by deflation.

(2) A change of surface roughness related to the vegetation cover (Tsoar and Pye, 1987). It is likely that the transition between coversand and loess was associated with a change in plant cover, which favourable for trapping the particles.

6.3. Pattern of dust production and accumulation

The geochemical analysis shows that northern and southern loess differ substantially in origin. For the latter, dust derived mainly from aeolian abrasion of the coversands (cf. Wright et al., 1998; Crouvi et al., 2010). Disconnection of the Landes plateau from the main drainage axes since at least the early Middle Pleistocene (Sitzia et al. 2015) due to tectonics resulted in intense redistribution of older alluvial sands by deflation and in the development of widespread coversands during the successive glacial periods. Repeated remobilization of the same aeolian sand stock together with fresh inputs from the continental shelf led to progressive enrichment of the sand material in minerals resistant to alteration (Legigan, 1979). The particle transport was predominantly NW-SE and the contribution of the alluvial plains, mainly oriented perpendicular to the wind, was low. The sand-loess transition is controlled by topography and coincides with the Adour valley (or the valleys of the tributaries).

In the northern part of the basin, dust came from aeolian abrasion of the coversands in the Blayais and the Plateau Girondin areas, and by deflation of alluvial material from the Garonne river. Channelling of the winds by the wide Garonne corridor and higher wind speeds favoured large dust production from the plain. Dust accumulated in the Entre-Deux-Mers area to form thick deposits mostly restricted to a narrow band on the valley side.

The loess thickness, which reaches at best 3.5 m in the south and 5 m in the Entre-Deux-Mers area, is low in comparison with values observed in other European regions (Lautridou, 1985; Haase et al., 2007). Several factors have been proposed to explain the low rate of accumulation (Bertran *et al.*, 2011): (1) a limited production of dust by aeolian abrasion of the coversands; (2) a narrow and steep continental shelf that does not allow storage of large amounts of fine alluvial sediment in the Garonne valley during sea lowstands; (3) a high soil moisture and, therefore, a low ground susceptibility to wind erosion due to an oceanic climate. The palaeoclimatic simulations both for LGM and MIS 3 agree to show that the average rainfall was significantly higher near the Atlantic coast than in Eastern Europe (Laîné et al., 2009; Kjellstrom et al., 2010; Strandberg *et al*., 2011; Sima et al., 2013) where much thicker loess deposits accumulated. However, this role remains questionable insofar as the reconstructed maximum in rainfall occurred in the winter season, which did not necessarily correspond to the most favourable period of aeolian transport.

6.4. Last-glacial wind regime from data and model constraints

The grain-size gradient together with the orientation of low-amplitude ridges and parabolic dunes allow reconstructing the prevailing wind directions of aeolian transport during the Last Glacial and the Lateglacial (Fig. 17A). The transverse ridges of the Plateau Girondin area dated to MIS 4-3 indicate efficient winds from the W. Some variability exists but appears to result from local topographical factors and from channelling of the air masses along the Garonne corridor. Unfortunately, the almost lack of MIS 2 ridge fields visible in aerial photographs does not allow getting data for this period. The crests of the MIS 2 ridges illustrated in Figure 4 are oriented W-E, and indicate local efficient winds blowing from the north. At the basin scale the contour lines of the grain size point to winds originating from the W or the NW, and are assumed to reflect the mean direction of efficient winds during the glacial. Finally, the parabolic dunes attest for winds coming from the W-SW during the YD. The following considerations must be taken into account with regard to the reconstruction of wind directions:

(1) The accuracy of the geological proxies used may vary. The dunes are considered as the best marker for the reconstruction of past wind circulation patterns (Lancaster, 1990), especially when dunes formed under unidirectional winds (Marrs and Kolm, 1982). With regard to grain-size gradients, Renssen et al. (2007) suggested that a significant uncertainty is associated with this type of feature. The analysis made here across the Aquitaine basin, however, shows a good consistency in the regional distribution of the contour lines.

(2) The reconstructed directions of aeolian transport are indicative of the wind regimes at the regional scale during the periods of accumulation. In most of the modern sand seas, the axis of unidirectional dunes is oriented perpendicular (e.g. barchan, transverse ridges, parabolic dunes) to the dominant wind direction, i.e. the direction with the highest transport rate of sand (Fryberger and Dean, 1979). Seasonal fluctuations in wind strength are assumed to be the main factor involved in modulating the intensity of deflation. In periglacial environments, however, wind intensity is not the only factor that controls the season of aeolian transport. Other factors, particularly the snow cover and soil moisture, play a significant role on the susceptibility of the ground to deflation (Koster, 1988; Seppälä, 2004). Depending on the temperature and precipitation regimes (also determining the vegetation), different situations exist. In cold and arid environments, based on observations in the Søndre Strømfjord region (West Greenland), Dijkmans and Törnqvis (1991) have shown that aeolian transport occurred mainly during part of the winter season, whereas summer was less favourable to deflation because of vegetation growth and ground-ice melting. Based on laboratory experiments, McKenna-Neuman (1989) also showed that the release of sand material susceptible to be transported by the wind can very active when the temperature drops below -20°C because of ice sublimation. On the contrary, between -5 and -15°C, the erosion threshold increases considerably due to the presence of a significant amount of liquid water in the ground. Dijkmans and Koster (1990), for Alaska, underline that when the snow cover is thick, the season of aeolian transport shifts towards the end of winter. According to Seppälä (2004), in

arctic and subarctic regions where snow is abundant, deflation is effective only during summer, i.e. after snowmelt.

In the following, we compare our proxy data and palaeoclimatic simulations in an attempt to specify the periods of the year when dust activity occurred during the investigated climate intervals. The result depends on how reliable the simulated variables, especially the wind directions, are. In the region studied here, the atmospheric circulation is largely determined by the surface conditions (temperatures, sea-ice extent) in the North Atlantic; in glacial times, another key factor was the size of the Laurentide ice sheet (e.g., Löfverström et al., 2014, Beghin et al., 2015). In our simulation for 21 ka, these elements are imposed from reconstructions for the LGM (GLAMAP, ICE-5G). Even though these reconstructions have their uncertainties, we tend to be confident in the general aspect of the modelled annual cycle of wind directions. For the 39 ka simulation, the sea-level drop is realistic and the ice-sheet configuration is adapted to this sea-level drop, the main uncertainty being related to the North-Atlantic surface conditions. Results of numerical experiments with the LOVECLIM earth system model of intermediate complexity (Van Meerbeeck et al., 2009) show a difference of air temperature of 3°C on average over the North Atlantic between an average MIS 3 stadial state and the LGM. For the MIS 3 run examined here, the difference is 2.5°C, close enough to the Van Meerbeeck et al. value, knowing that there was no unique (or average) MIS 3 stadial climate, but many stadial episodes differing in ice-sheet size and orbital parameters.

Since we are reasonably confident in the simulated wind directions, constraints on the dusty season can be derived using the comparison between the modelled wind directions and those reconstructed from field proxies, together with the results of sensitivity experiments with lower roughness length more typical of glacial vegetation. The only other constraining element that we can use is the simulated soil moisture, keeping in mind that it is underestimated in the cold part of the year.

In the LGM simulation, soil moisture conditions allow dust activity to start in the beginning of March, while reconstructed W-NW wind directions suggest that the dusty season should not begin before mid-March, when simulated winds change from W-SW to W (Fig. 17A). Sand transport took place during the spring/summer times because of scarce vegetation, adequate wind speeds and well-drained sandy soils. According to recent investigations

(Andrieux et al., 2016), permafrost, which might have impeded drainage (Kasse, 1997), was lacking during most of the period of sand accumulation. Deflation may have been more restricted in summer in the loess area because of the denser vegetation cover. This scenario contrasts with that proposed by Renssen et al. (2007) for more northern latitudes, which suggested winter to be the most suitable period for deflation during MIS 2. In such a permafrost context and by comparison with the modern periglacial environments investigated by Dijkmans (1990) and Dijkmans and Törnqvist (1991), deflation was thought to have been impeded during the summer because the ground was mostly wet (thaw of the active layer), vegetation was growing, and the wind speeds were lower than in the winter season. It is worth noting that the observations in modern milieus were made on aeolian systems supplied by proglacial rivers. These rivers fed by glaciers are mostly active after the spring melt. In summer, the water table rises and, as a consequence, the sediment availability to deflation is low (Mountney and Russell, 2009). Such an aeolian system was probably characteristic of the margins of the Scandinavian ice sheet (Koster, 1988), but cannot be transposed to regions far from an ice sheet such as the Aquitaine basin. In this oceanic region, the ground was wet and largely protected by a snow cover (largely underestimated in our simulation) during the passage of winter storms, but dried in summer, thus becoming more susceptible for deflation.

In the MIS 3 simulation, the soil becomes dry enough in the beginning of March, while the reconstructed westerly winds suggest that the dusty season should not begin before the end of March. Both data and model agree that the dust activity should cease in the end of May, when the simulated winds turn from W (which is the reconstructed direction) to WNW, and the maximum wind speeds, recalculated with a roughness length value more typical of steppe vegetation (green curve in Fig. 17D), become too weak. The modelled wind directions coincide again with the reconstructed (westerly) ones in autumn, but the simulated increase in soil moisture suggests that little, if any, dust activity should occur.

Wind strength, soil moisture and snow cover determine the dusty season(s) in scarcely vegetated environments, Where vegetation has strong seasonal variations, its impact is also important. The developing vegetation contributes to wind weakening through increasing roughness length, and protects the surface against erosion, The later effect cannot be estimated here due to the unrealistically high vegetation cover in the study region, but Sima et al. (2009) have found that it stopped dust activity in the warm season under MIS 3 conditions in Europe at latitudes around 50°N.

We do not have a simulation for the YD, but we note that the annual cycle of wind direction does not considerably change between present day, LGM and MIS 3 (in our simulations, also in those by van Huissteden and Pollard 2003), and even from the present day. Therefore, we may speculate that winter, typified by dominantly W-SW wind directions, was the main period of sand transport during the YD. In Western Europe, winter is the season that corresponds to the passage of the main perturbations and associated storms, and that records the highest wind speeds (Fig. 17C, D). These wind directions are in agreement with those reconstructed for the YD by Isarin et al. (1997). The YD orientation of parabolic dunes in Aquitaine is identical to that observed in the Netherlands (Isarin et al., 1997) and should be associated with increased speed of SW winds throughout Northwestern and Western Europe (Isarin et al., 1997). Differences should have been important in the surface conditions, which for the YD allowed dust activity in winter: scarce vegetation, reduced snow cover compared to LGM and MIS 3, and reduced soil moisture favoured by improved ground drainage due to the lack of permafrost and to the weaker influence of meltwater from the ice sheets (for Northern Europe).

7. Conclusions

The multi-approach study of the aeolian deposits of southwest France allows better understanding of sediment sources and depositional dynamics. The maps of interpolated grain size and the geochemical composition converge to show a genetic relationship between coversands and finer-grained deposits. In the southern part of the basin, dust derived mainly from aeolian abrasion of the coversands and is dominantly composed of minerals resistant to alteration. In contrast, both the coversands and the floodplain of the Garonne river, richer in Ca-bearing minerals, contributed to loess in the northern part of the basin.

The low-amplitude dunes lacking slipfaces, dated to MIS 4-3, are interpreted as zibars and show variable morphologies (transverse, barchanoid, isolated barchanoid) occurring as strips subparallel to the coastline. This pattern seems to be mainly controlled by the slope gradient. The parabolic dunes dated to the YD are simple, complex or compound. These are clustered along the rivers but are rare on the plateaus, which correspond to deflation areas. In the valleys oriented W-E, i.e. parallel to the prevailing winds, corridors of elongated parabolic dunes developed, whereas more simple shapes occur on both sides of the valleys perpendicular to the winds. These formed as a consequence of relief-induced deceleration of the airflows. Overall, the dune distribution indicates that the sand supply came mainly from the coast.

The spatial analysis of dune shapes and grain-size gradients, as well as the study of dust sources, made it possible reconstructing the Last Glacial wind regimes in the study region. The efficient winds changed significantly through time. They came from the W to the NW during the glacial, and the W-SW during the YD. The comparison between proxy data and both the current and simulated Last Glacial wind regimes strongly suggests that aeolian transport of sand and dust occurred mostly during the spring/summer season for the glacial, and the winter for the YD. We assume that these variations were not related to changes in the pattern of atmospheric circulation, but rather to changes in the deflation season. This was mainly controlled by the length of the season with a snow cover and frozen or moist ground, and by the seasonal evolution of the wind speeds able to cause deflation. Vegetation could impose additional constraints in areas or periods when its seasonal variations were significant.

Acknowledgments

We acknowledge Christophe Tuffery (Inrap) for his help in the GIS. This work was funded by Inrap, the University of Bordeaux and Lascarbx (Universités de Bordeaux, program of the Agence Nationale de la Recherche ANR-10-LABX-52). The Labex L-IPSL, which is funded by the ANR (grant #ANR-10-LABX-0018), is also acknowledged. The two anonymous reviewers are also thanked for their remarks, which contributed to greatly improve the manuscript. The simulations used here have been run on the HPC facilities of the Commissariat à l’Energie Atomique.

References

Aitchison, J., 1982. The Statistical Analysis of Compositional Data. Journal of the Royal Statistical Society, s eries B (Methodological) 44, 139–177.

Aitchison, J., 1986. The Statistical Analysis of Compositional Data. Chapman & Hall, London, UK, 416 pp.

Aitchison, J., Greenacre, M., 2002. Biplots of compositional data. Journal of the Royal Statistical Society, series C (Applied Statistics) 51, 375–392.

Andrieux, E., Bertran, P., and Saito, K., 2016. Spatial analysis of the French Pleistocene permafrost by a GIS database. Permafrost and Periglacial Processes 27, 17–30.

Antoine, P., Rousseau, D.-D., Zöller, L., Lang, A., Munaut, A.-V., Hatté, C., Fontugne, M., 2001. High-resolution record of the last Interglacial-glacial cycle in the Nussloch loess-palaeosol sequences, Upper Rhine Area, Germany. Quaternary International 76-77, 211–229.

Appelman F., 1956. Variation de la composition granulométrique des sédiments éoliens en rapport avec leur latitude et leur altitude. Pédologie VI, 26–37.

Ballabio, C., Panagos, P., Monatanarella, L., 2016. Mapping topsoil physical properties at European scale using the LUCAS database. Geoderma 261, 110-123.

Bagnold, R.A., 1941. The physics of wind blown sand and desert dunes. Methuen, London, 265 pp.

Banks, W. E., Zilhão, J., d'Errico, F., Kageyama, M., Sima, A., & Ronchitelli, A. (2009). Investigating links between ecology and bifacial tool types in Western Europe during the Last Glacial Maximum. Journal of Archaeological Science, 36, 2853-2867.

Barchyn, T.E., Hugenholtz, C.H., 2013. Reactivation of supply-limited dune fields from blowouts: A conceptual framework for state characterization. Geomorphology 201, 172–182.

Berger, A., 1978. Long-term variations of caloric solar radiation resulting from the earth's orbital elements. Quaternary Research 9, 139–167.

Bertran, P., Allenet, G., Gé, T., Naughton, F., Poirier, P., Goñi, M.F.S., 2009. Coversand and Pleistocene palaeosols in the Landes region, southwestern France. Journal of Quaternary Science 24, 259–269.

Bertran, P., Bateman, M.D., Hernandez, M., Mercier, N., Millet, D., Sitzia, L., Tastet, J.-P., 2011. Inland aeolian deposits of south-west France: facies, stratigraphy and chronology. Journal of Quaternary Science 26, 374–388.

Bertran, P., Andrieux, E., Antoine, P., Coutard, S., Deschodt, L., Gardère, P., Hernandez, M., Legentil, C., Lenoble, A., Liard, M., Mercier, N., Moine, O., Sitzia, L., Van Vliet-Lanoë, B., 2013. Distribution and chronology of Pleistocene permafrost features in France: database and first results. Boreas 43. 699-711.

Bertran, P., Liard, M., Sitzia, L., Tissoux, H., 2016. A map of Pleistocene aeolian deposits in Western Europe, wiht special emphasis on France. Journal of Quaternary Science 31 (8), 844-856.

Braconnot, P., 2004. Modeling the last glacial maximum and mid-holocene. Comptes Rendus Geoscience 336, 711–719.

Buurman, P., Pape, T., Reijneveld, J.A., de Jong, F., van Gelder, E., 2001. Laser-diffraction and pipette-method grain sizing of Dutch sediments: correlations for fine fractions of marine, fluvial, and loess samples. Netherlands Journal of Geosciences 80, 49-57.

Capdeville J.-P., Dubreuilh J., 1994. Les formations superficielles du Bassin d'Aquitaine: identification, potentialités, contraintes. BRGM report R-38 271, Orléans, 52 pp.

Comas-Cufí, M., Thió-Henestrosa, S., 2011. CoDaPack 2.0: A stand-alone, multi-platform compositional software. http://ima.udg.edu/codapack/ (accessed 06/07/2016).

Conseil régional Aquitaine et ADEME Aquitaine, 2008. Cartographie du gisement éolien, des contraintes et servitudes en Aquitaine, Unpublished Report, 27 pp.

Cooke, R.U., Warren, A., 1973. Geomorphology in Deserts. University of California Press, 448 pp.

Crouvi, O., Amit, R., Enzel, Y., Gillespie, A.R., 2010. Active sand seas and the formation of desert loess. Quaternary Science Reviews 29, 2087–2098.

De Vos, W., Tarvainen, T., Salminen, R., Reeder, S., De Vivo, B., Demetriades, A., Pirc, S., Batista, M.J., Marsina, K., Ottesen, R.T., O'Connor, P.J., Bidovec, M., Lima, A., Siewers, U., Smith, B., Taylor, H., Shaw, R., Salpeteur, I., Gregorauskiene, V., Halamic, J., Slaninka, I., Lax, K., Gravesen, P., Birke, M., Breward, N., Ander, E.L., Jordan, G., Duris, M., Klein, P., Locutura, J., Bel-lan, A., Pasieczna, A., Lis, J., Mazreku, A., Gilucis, A., Heitzmann, P., Klaver, G., Petersell, V., 2006. Geochemical Atlas of Europe. Part 2 - Interpretation of Geochemical Maps, Additional Tables, Figures, Maps, and Related Publications, Geological Survey of Finland, Espoo.

Dijkmans, J.W.A., Koster, E.A., 1990. Morphological Development of Dunes in a Subarctic Environment, Central Kobuk Valley, Northwestern Alaska. Geografiska Annaler. Series A, Physical Geography 72, 93–109.

Dijkmans, J.W.A., Törnqvist, T.E., 1991. Modern periglacial eolian deposits and landforms in the Søndre Strømfjord area, West Greenland and their palaeoenvironmental implications. Meddelelser om Grønland. Geoscience 25, 3–39.

Dubreuilh, J., 1976. Contribution à l'étude sédimentologique du système fluviatile Dordogne-Garonne dans la région bordelaise. Thèse d'état, Université de Bordeaux, Bordeaux, 273 pp.

Dubreuilh, J., Capdeville, J.P., Farjanel, G., Karnay, G., Platel, J.P., Simon-Coinçon, R., 1995. Dynamique d'un comblement continental néogène et quaternaire: l'exemple du bassin d'Aquitaine. Géologie de la France 4, 3–26.

Duchaufour, P., 1997. Abrégé de pédologie : sol, végétation, environnement. Masson, Paris, 285 pp.

Enjalbert, H., 1960. Les Pays Aquitains : Le modelé et les sols. Imprimerie Bière, Bordeaux.

Egozcue J., Pawlowsky-Glahn, V., Mateu-Figueras, G., Barceló- Vidal, C., 2003. Isometric logratio transformations for compositional data analysis. Mathematical Geology 35, 3, 279–300.

Ewing, R.C., Kocurek, G., Lake, L.W., 2006. Pattern analysis of dune - field parameters. Earth Surface Processes and Landforms 31, 1176–1191.

Fralick B.W., Kronberg B.I., 1997. Geochemical discrimination of clastic sedimentary rock sources. Sedimentary Geology 113, 111-124.

Frazee, C.J., Fehrenbacher, J.B., Krumbein, W.C., 1970. Loess Distribution from a Source. Soil Science Society of America Journal 34, 296–301.

Fryberger, S.G., Dean, G., 1979. Dune forms and wind regime, in: McKee, E.D. (Ed.), A Study of Global Sand Seas, Geological Survey Professional Paper 1052, United States Government Printing Office Washington DC, p. 137–171.

Gallet, S., Jahn, B., Van Vliet Lanoë, B., Dia, A., Rossello, E., 1998. Loess geochemistry and its implications for particle origin and composition of the upper continental crust. Earth and Planetary Science Letters 156, 157–172.

Haase, D., Fink, J., Haase, G., Ruske, R., Pécsi, M., Richter, H., Altermann, M., Jäger, K.-D., 2007. Loess in Europe--its spatial distribution based on a European Loess Map, scale 1:2.500.000. Quaternary Science Reviews 26, 1301–1312.

Hernandez, M., Mercier, N., Bertran, P., Colonge, D., Lelouvier, L.A., 2012. Premiers éléments de datation des industries du Pléistocène moyen (Acheuléen - Paléolithique moyen ancien) de la région pyrénéo-garonnaise : une approche géochronologique pluri-méthodes (TL, OSL et TT-OSL) des sites de Duclos et Romentères. Paléo 23, 155–170.

Hesp, P., 2002. Foredunes and blowouts: initiation, geomorphology and dynamics. Geomorphology 48, 245–268.

Holm, D.A., 1960. Desert Geomorphology in the Arabian Peninsula. Science 132, 1369–1379.

INRA, 2011. Donesol version 2.0.5. http://acklins.orleans.inra.fr/outil/donesol/dictionnaire_donesol_igcs_2011-02-25.pdf (accessed 05.07.2016).

Isarin, R.F.B., Renssen, H., Koster, E.A., 1997. Surface wind climate during the Younger Dryas in Europe as inferred from aeolian records and model simulations. Palaeogeography, Palaeoclimatology, Palaeoecology 134, 127-148.

Karnay, G., Corbier, P., Bourgine, B., Saltel M., 2010. Gestion des eaux souterraines en région Aquitaine. Reconnaissance des potentialités aquifères du Mio-Plio-Quaternaire des Landes de Gascogne et du Médoc en relation avec les SAGE. BRGM report RP 57813, Orléans, 73 pp.

Kasse, C., 1997. Cold-Climate Aeolian Sand-Sheet Formation in North-Western Europe (c. 14–12.4 ka); a Response to Permafrost Degradation and Increased Aridity. Permafrost and Periglacial Processes 8, 295–311.

Kjellström, E., Brandefelt, J., Näslund, J.-O., Smith, B., Strandberg, G., Voelker, A. H. L., Wohlfarth, B., 2010. Simulated climate conditions in Europe during the Marine Isotope Stage 3 stadial. Boreas 39: 436–456.

Klingebiel, A., 1966. Observations sur les sables de recouvrement superficiel dans le bordelais. Bulletin de la carte géologique de la France, t. LXI, 278, 185–188.

Kocurek, G., Nielson, J., 1986. Conditions favourable for the formation of warm-climate aeolian sand sheets. Sedimentology 33, 795–816.

Konert, M., Vandenberghe, J., 1997. Comparison of laser grain size analysis with pipette and sieve analysis: a solution for the underestimation of the clay fraction. Sedimentology 44, 523–535.

Koster, E.A., 1988. Ancient and modern cold-climate aeolian sand deposition: A review. Journal of Quaternary Science 3, 69–83.

Krinner, G., Viovy, N., de Noblet-Ducoudré, N., Ogée, J., Polcher, J., Friedlingstein, P., Ciais, P., Sitch, S., Prentice, I.C., 2005. A dynamic global vegetation model for studies of the coupled atmosphere-biosphere system. Global Biogeochemical Cycles 19, GB1015.

Kutzbach, J.E., Wright Jr., H.E., 1985. Simulation of the climate of 18,000 years BP: results for the North American/North Atlantic/European sector and comparison with the geologic record of North America. Quaternary Science Reviews 4, 147–187.

Laîné A., Kageyama M., Salas-Mélia D., Valdoire A., Rivière G., Ramstein G., Planton S., Tyteca S., Peterschmidtt J.Y., 2009. Northern Hemisphere storm tracks during the last glacial maximum in the PMIP2 ocean-atmosphere coupled models: energy study, seasonal cycle, precipitation. Climate Dynamics 32, 593-614.

Lancaster, N., 2008. Desert dune dynamics and development: insights from luminescence dating. Boreas 37, 559–573.

Lancaster, N., 1995. Geomorphology of desert dunes. Routledge physical environment series, K. Richards (ed.), Routledge, London, New York, 290 pp.

Lancaster, N., 1990. Palaeoclimatic evidence from sand seas. Palaeogeography, Palaeoclimatology, Palaeoecology 76, 279–290.

Lancaster, N., Kocurek, G., Singhvi, A., Pandey, V., Deynoux, M., Ghienne, J.-F., Lo, K., 2002. Late Pleistocene and Holocene dune activity and wind regimes in the western Sahara Desert of Mauritania. Geology 30, 991–994.

Lautridou, J.-P., 1985. Le cycle périglaciaire pleistocène en Europe du nord-ouest et plus particulièrement en Normandie. Thèse d'état, Université de Caen, Centre de géomorphologie du C.N.R.S, Caen, France, 908 pp.

Léger, M., 1990. Loess landforms. Quaternary International 7/8, 53-61.

Legigan, P., 1979. L'élaboration de la formation du Sable des Landes, Mémoire de l'Institut de Géologie du Bassin d'Aquitaine, Bordeaux, 429 pp.

Liu, T., 1988. Loess in China. Springer series in physical environment, Springer, Berlin, 224 pp.

Löfverström, M., Caballero, R., Nilsson, J., Kleman, J., 2014. Evolution of the large-scale atmospheric circulation in response to changing ice sheets over the last glacial cycle, Climate of the Past 10, 1453-1471, doi: 10.5194/cp-10-1453-2014.

Maarleveld, G.C., 1960. Wind directions and cover sands in the Netherlands. Biuletyn Peryglacjalny 8, 49–58.

Marrs, R.W., Kolm, K.E. (Eds.), 1982. Interpretation of windflow characteristics from eolian landforms, Special paper 192, Geological society of America, Boulder, USA, 109 pp.

Martín-Fernández, J., Barceló-Vidal, C., Pawlowsky-Glahn, V., 2003. Dealing with Zeros and Missing Values in Compositional Data Sets Using Nonparametric Imputation. Mathematical Geology 35, 253–278.

Mason, J.A., 2001. Transport Direction of Peoria Loess in Nebraska and Implications for Loess Sources on the Central Great Plains. Quaternary Research 56, 79–86.

Mason, J.A., Nater, E.A., Zanner, C.W., Bell, J.C., 1999. A new model of topographic effects on the distribution of loess. Geomorphology 28, 223–236.

McKee, E.D., 1979. Introduction to a study of global sand seas, in: E.D. McKee (ed.), A Study of Global Sand Seas, Geological Survey Professional Paper 1052, United States Government Printing Office Washington DC, pp. 1–19.

McKenna Neuman, C., 1989. Kinetic energy transfer through impact and its role in entrainment by wind of particles from frozen surfaces. Sedimentology 36, 1007–1015.

Melkerud P.A., Bain D.C., Jongmans A.G., Tarvainen T., 2000. Chemical, mineralogical and morphological characterization of three podzols developed on glacial deposits in Northern Europe. Geoderma 94, 125-148.

Mountney, N.P., Russell, A.J., 2009. Aeolian dune - field development in a water table controlled system: Skeiđarársandur, Southern Iceland. Sedimentology 56, 2107–2131.

Muhs, D.R., Bettis, E.A., Aleinikoff, J.N., McGeehin, J.P., Beann, J., Skipp, G., Marshall, B.D., Roberts, H.M., Johnson, W.C., Benton, R., 2008. Origin and paleoclimatic significance of late Quaternary loess in Nebraska: Evidence from stratigraphy, chronology, sedimentology, and geochemistry. Geological Society of America Bulletin 120, 1378–1407.

Nielson, J., Kocurek, G., 1986. Climbing Zibars of the Algodones. Sedimentary Geology 48, 1–15.

Pannatier, Y., 1996. Variowin : software for spatial data analysis in 2D, Statistics and computing. Springer, New York, Berlin, London, Paris, 91 pp.

Park, S.-U., In, H.-J., 2003. Parameterization of dust emission for the simulation of the Yellow Sand (Asian dust) observed in March 2002 in Korea. Journal of Geophysical Research 108, 4618, doi:10.1029/2003JD003484.

Paul, A., Schäfer-Neth, C., 2003. Modeling the water masses of the Atlantic Ocean at the Last Glacial Maximum. Paleoceanography 18, 1058.

Pawlowsky-Glahn, V., Buccianti, A., 2011. Compositional Data Analysis: Theory and Applications. John Wiley & Sons, Chichester, 378 pp.

Pawlowsky-Glahn, V., Olea, R.A., 2004. Geostatistical analysis of compositional data. Oxford University Press, Oxford, 204 pp.

Pawlowsky, V., Burger, H., 1992. Spatial structure analysis of regionalized compositions. Mathematical Geology 24, 675–691.

Peltier W.R., 2004. Global glacial isostasy and the surface of the ice-age earth: the ICE-5G (VM2) Model and GRACE Annual Review of Earth and Planetary Sciences 32, 111-149.

Poser, H., 1950. Zur Rekonstruktion der spätglazialen Luftdruckverhältnisse in Mittelund Westeuropa auf Grund der vorzeitlichen binnenDünen. Erdkunde 4, 81–88.

Pye, K., 1982. Morphological Development of Coastal Dunes in a Humid Tropical Environment, Cape Bedford and Cape Flattery, North Queensland. Geografiska Annaler. Series A, Physical Geography 64, 213–227.

Pye, K., Tsoar, H., 2009. Aeolian sand and sand dunes. Springer, Berlin, Heidelberg, 458 pp.

Raynaud, D., Jouzel, J., Barnola, J.M., Chapellaz, J., Delmas, R.J., Lorius, C., 1993. The ice record of greenhouse gases. Science 259, 926–934.

Reimann C., Demetriades A., Birke M., Filzmoser P., O'Connor P., Halamić J., Ladenberger A., The GEMAS Project Team, 2014. Distribution of elements/parameters in agricultural and grazing land soil of Europe. In C. Reimann, M. Birke, A. Demestriades, P. Filzmoser & P. O'Connor, Chemistry of Europe's agricultural soils, Part A: Methodology and interpretation of the GEMAS Data Set, Geologisches Jahrbuch, Reihe B, 102, 103-523.

Renssen, H., Kasse, C., Vandenberghe, J., Lorenz, S.J., 2007. Weichselian Late Pleniglacial surface winds over northwest and central Europe: a model–data comparison. Journal of Quaternary Science 22, 281–293.

Righi D., De Coninck F., 1974. Micromorphological aspects of Humods and Haplaquods of the Landes du Médoc, France. in: Rutherford, G.K. (Ed.), Soil Microscopy. Limestone Press, Kingston, Ontario, pp. 567– 588.

Rousseau D.D., Chauvel C., Sima A., Hatté C., Lagroix F., Antoine P., Balkanski Y., Fuchs M., Mellett C., Kageyama M., Ramstein G., Lang A., 2014. European Glacial Dust Deposits: Geochemical Constraints on Atmospheric Dust Cycle Modeling. Geophysical Research Letters 41, 7666-7674. doi : 10.1002/2014GL061382

Ruegg, G.H.J., 1983. Periglacial Eolian Evenly Laminated Sandy Deposits in the Late Pleistocene of Nw Europe, A Facies Unrecorded in Modern Sedimentological Handbooks, in: Developments in Sedimentology. Elsevier, pp. 455–482.

Sarnthein, M., Gersonde, R., Niebler, S., Pflaumann, U., Spielhagen, R., Thiede, J., Wefer, G., Weinelt, M., 2003. Overview of Glacial Atlantic Ocean Mapping (GLAMAP 2000). Paleoceanography 18, 1030.

Scheib A.J., Birke M., Dinelli E., GEMAS Project Team, 2014. Geochemical evidence of aeolian deposits in European soils. Boreas 43, 175-192.

Schwan, J., 1986. The origin of horizontal alternating bedding in weichselian aeolian sands in Northwestern Europe. Sedimentary Geology 49, 73–108.

Seppälä, M., 2004. Wind as a geomorphic agent in cold climates. Cambridge University press, Cambridge, 358 pp..

Sima, A., Rousseau, D.-D., Kageyama, M., Ramstein, G., Schulz, M., Balkanski, Y., Antoine, P., Dulac, F., Hatté, C., 2009. Imprint of North-Atlantic abrupt climate changes on western European loess deposits as viewed in a dust emission model. Quaternary Science Reviews 28, 2851–2866.

Sima, A., Kageyama, M., Rousseau, D.-D., Ramstein, G., Balkanski, Y., Antoine, P., and Hatté, C., 2013. Modeling dust emission response to North Atlantic millennial-scale climate variations from the perspective of East European MIS 3 loess deposits, Climate of the Past 9, 1385-1402.

Simonson R.W., Hutton C.E., 1954. Distribution curves for loess. American Journal of Science 252, 99–105.

Sitzia, L., 2014. Chronostratigraphie et distribution spatiale des dépôts éoliens du Bassin Aquitain. PhD Thesis, Université de Bordeaux, Bordeaux, 341 pp.

Sitzia, L., Bertran, P., Bahain, J.-J., Bateman, M.D., Hernandez, M., Garon, H., de Lafontaine, G., Mercier, N., Leroyer, C., Queffelec, A., Voinchet, P., 2015. The Quaternary coversands of southwest France. Quaternary Science Reviews 124, 84–105.

Stevens, T., Palk, C., Carter, A., Lu, H., Clift, P.D., 2010. Assessing the provenance of loess and desert sediments in northern China using U-Pb dating and morphology of detrital zircons. Geological Society of America Bulletin 122, 1331–1344.

Strandberg G., Brandefelt J., Kjellström E., Smith B., 2011. High resolution simulation of last glacial maximum climate in Europe. Tellus 63 A, 107-125.

Sun, J., Muhs, D.R., 2007. Dune Fields | Mid-Latitudes, in: Elias, S.A. (Ed.), Encyclopedia of Quaternary Science. Elsevier, Oxford, pp. 607–626.

Taylor, S.R., McLennan, S.M., 1995. The geochemical evolution of the continental crust. Reviews of Geophysics 33, 241-265.

Thibault, C., 1970. Recherches sur les terrains quaternaires du bassin de l'Adour. Thèse d'état, Université de Bordeaux, Bordeaux, 814 pp.

Tsoar, H., 1978. The Dynamics of Longitudinal Dunes. (Final technical report). DTIC Document, London: European Research Office, US Army, 171 pp.

Tsoar, H., Pye, K., 1987. Dust transport and the question of desert loess formation. Sedimentology 34, 139–153.

Van Huissteden, Ko (J), Schwan, J.C.G., Bateman, M.D., 2001. Environmental conditions and paleowind directions at the end of the Weichselian Late Pleniglacial recorded in aeolian sediments and geomorphology (Twente, Eastern Netherlands). Geologie en Mijnbouw / Netherlands Journal of Geosciences 80, 1–18.

van Huissteden, K.., Pollard, D., 2003. Oxygen isotope stage 3 fluvial and eolian successions in Europe compared with climate model results. Quaternary Research 59, 223–233.

van Meerbeeck, C.J., Renssen, H., Roche, D.M., 2009. How did Marine Isotope Stage 3 and Last Glacial Maximum climates differ? – Perspectives from equilibrium simulations. Climate of the Past 5, 33-51.

Waggoner P.E., Bingham C., 1961. Depth of loess and distance from source. Soil Science 92, 396–401.

Warren, A., 1972. Observations on Dunes and Bi-Modal Sands in the Ténéré Desert. Sedimentology 19, 37–44.

Webster, R., Oliver, M.A., 2007. Geostatistics for environmental scientists. Statistics in practice. Wiley, Chichester, 315 pp.

Wedepohl, K.H., 1978. Handbook of geochemistry. Springer-Verlag, Berlin, Heidelberg, 443 pp.

Wiggs, G., Bullard, J., Garvey, B., Castro, I., 2002. Interactions Between Airflow and Valley Topography with Implications for Aeolian Sediment Transport. Physical Geography 23, 366–380.

Wojdyr M. J., 2010 : *Fityk*: a general-purpose peak fitting program. Journal of Applied Crystallography, 43, p. 1126-1128.

Wolfe, S., 2004. Relict Late Wisconsinan Dune Fields of the Northern Great Plains, Canada. Géographie physique et Quaternaire 58, 323–336.

Wolfe, S.A., Moorman, B.J., Hugenholtz, C.H., 2008. Effects of sand supply on the morphodynamics and stratigraphy of active parabolic dunes, Bigstick Sand Hills, southwestern Saskatchewan. Canadian Journal of Earth Sciences 45, 321–335.

Wright, J., Smith, B., Whalley, B., 1998. Mechanisms of loess-sized quartz silt production and their relative effectiveness: laboratory simulations. Geomorphology 23, 15–34.

Wu, H., Guiot, J., Brewer, S., Guo, Z., 2007. Climatic changes in Eurasia and Africa at the last glacial maximum and mid-Holocene: reconstruction from pollen data using inverse vegetation modelling. Climate Dynamics 29, 211–229.

Zeeberg, J., 1998. The European sand belt in Eastern Europe - and comparison of Late Glacial dune orientation with GCM simulation results. Boreas 27, 127–139.

Figures

Fig. 1: European aeolian deposits. A – General map from Bertran et al. (2016) and location of the study area; B – Close-up view of southwest France. The distribution of ventifacts is from Bertran et al. (2011).

Fig. 2: Modern meteorological parameters in the studied area. A - Roses of seasonal winds in Aquitaine (period 1999-2007) according to MétéoFrance (Ile d'Yeu weather station); B - Mean wind speeds ($m.s^{-1}$) at a height of 80 m, from Agri4cast (2016); the dashed line indicates the coversand limit.

Fig. 3: A, B - Detailed topography of barchanoid ridges (photogrammetry); location shown in Figure 4A. pr – Pleistocene ridge field; hs: Holocene sand cover at the front of a parabolic dune. North to the top. A', B' – Aerial views of the same areas (photos IGN / Google Earth).

Fig. 4: View of transverse ridges dated to MIS 2, Pontonx-sur-l'Adour.

Fig. 5: Ridges of the Plateau Girondin. A – Distribution of low-amplitude ridges (zibars) and orientation of the vector perpendicular to dune crests. B – Topographic transect between the Atlantic coast and the Garonne river, and associated dunes morphologies. C – Photo-mosaic of fields showing low-amplitude ridges (photos IGN / Google Earth) with superimposed 5 m contour lines, and close-up view of ridge fields.

Fig. 6: Distribution of parabolic dunes (in red) according to the 1:50,000 geologic map (Bureau des Recherches Géologiques et Minières) and orientation of the bisector of the angle between the two arms for simple and complex dunes. The rectangles indicate the location of figures 6A-D.

Fig. 7: Parabolic dunes, 5 m DEM (RGE Alti® 2.0, IGN 2014). The areas represented are shown in Figure 5. A – Dunes (indicated by white arrows) on both left and right banks of a river; B – Compound elongated parabolic dune; C - Parabolic dunes on the right (i.e. wind-facing) bank of a river; D - Dunes on the left bank of a river.

Fig. 8: Grain-size maps of the aeolian deposits interpolated by ordinary kriging. The white dots correspond to the sites used for kriging. The dotted line indicates the coversand limit.

Fig. 9: Detailed maps of the coarse (upper panel) and fine (bottom panel) silt content in the northern (A) and the southern (B) part of the Aquitaine basin.

Fig. 10: Evolution of the grain-size mode of some representative samples from the southern part of the basin. The modes were established after deconvolution of the grain-size curves using the software Fityk 0.9.8 (Wojdyr, 2010). The location of the samples is shown in Figure 8.

Fig. 11: Grain size distribution of some representative samples of sandy silts and loess from the Landes district. The location of the samples is shown in Figure 8.

Fig. 12: Map of the thickness of the loess located on the right bank of the Garonne river (A) and on the left bank of the Adour river (B). The coversand limit is indicated by a dashed line.

Fig. 13: Maps of the content in some elements of the aeolian and alluvial deposits. Fines = silt + clay.

Fig. 14: Ti, Zr, K and Al – Si scattergrams of aeolian and alluvial samples of the Aquitaine basin. UCC: upper continental crust composition according to Taylor and McLennan (1995). a – adjustment line for loess and the alluvial deposits of the Leyre and Ciron rivers; b – adjustment line for other alluvial deposits.

Fig. 15: Principal component analysis adapted to compositional data (“compositional biplot”) of major and minor elements (fraction > 63 µm) of aeolian and potential source deposits.

Fig. 16: Compositional biplot of major and minor elements (fraction < 63 µm) of aeolian and potential sources deposits.

Fig.17: Annual cycle of surface winds and ground conditions for the LGM and MIS 3 simulations (averaged over the domain between longitude 2°W-1°E and latitude 43°-45.5°N,

and over 20 years for each run). From top to bottom: wind direction, daily maximum wind speed for different values of roughness length (z0), and ground conditions (dry soil depth and percent of snow-free surface). Red dashed lines mark the different thresholds discussed in the text. Red rectangles indicate the most probable period of deflation according to the available constraints.

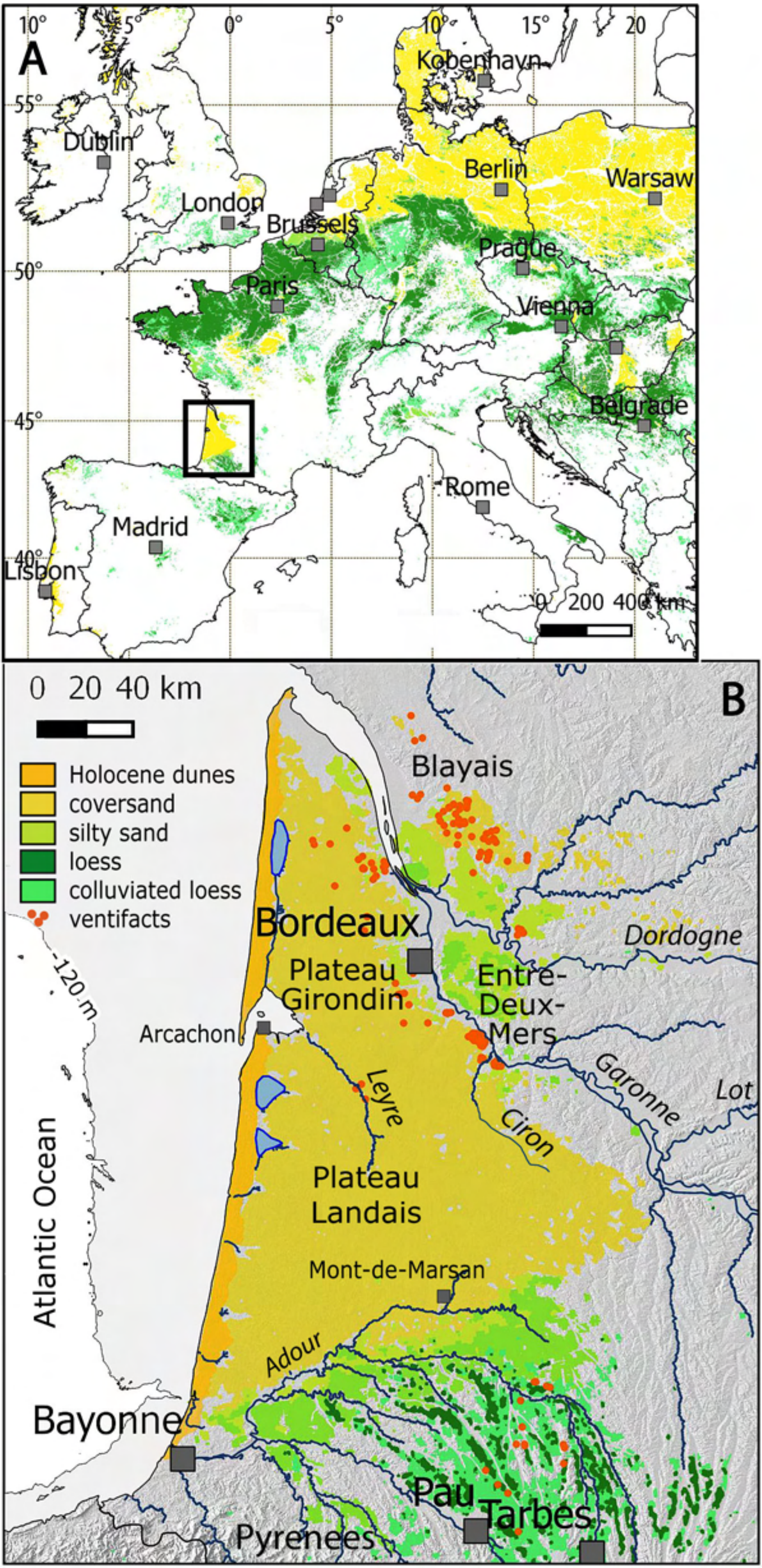
A
10°
5°
0°
5°
10°
15°
20
55°
50°
45°
40°
Kobenhavn
Dublin
Berlin
Warsaw
London
Brussels
Prague
Paris
Vienna
Belgrade
Rome
Madrid
Lisbon
0 200 400 km
B
0 20 40 km
Holocene dunes
coversand
silty sand
loess
colluviated loess
ventifacts
Blayais
Bordeaux
Plateau Girondin
Entre-Deux-Mers
Dordogne
-120 m
Arcachon
Leyre
Garonne
Lot
Ciron
Atlantic Ocean
Plateau Landais
Mont-de-Marsan
Adour
Bayonne
Pau
Tarbes
Pyrenees

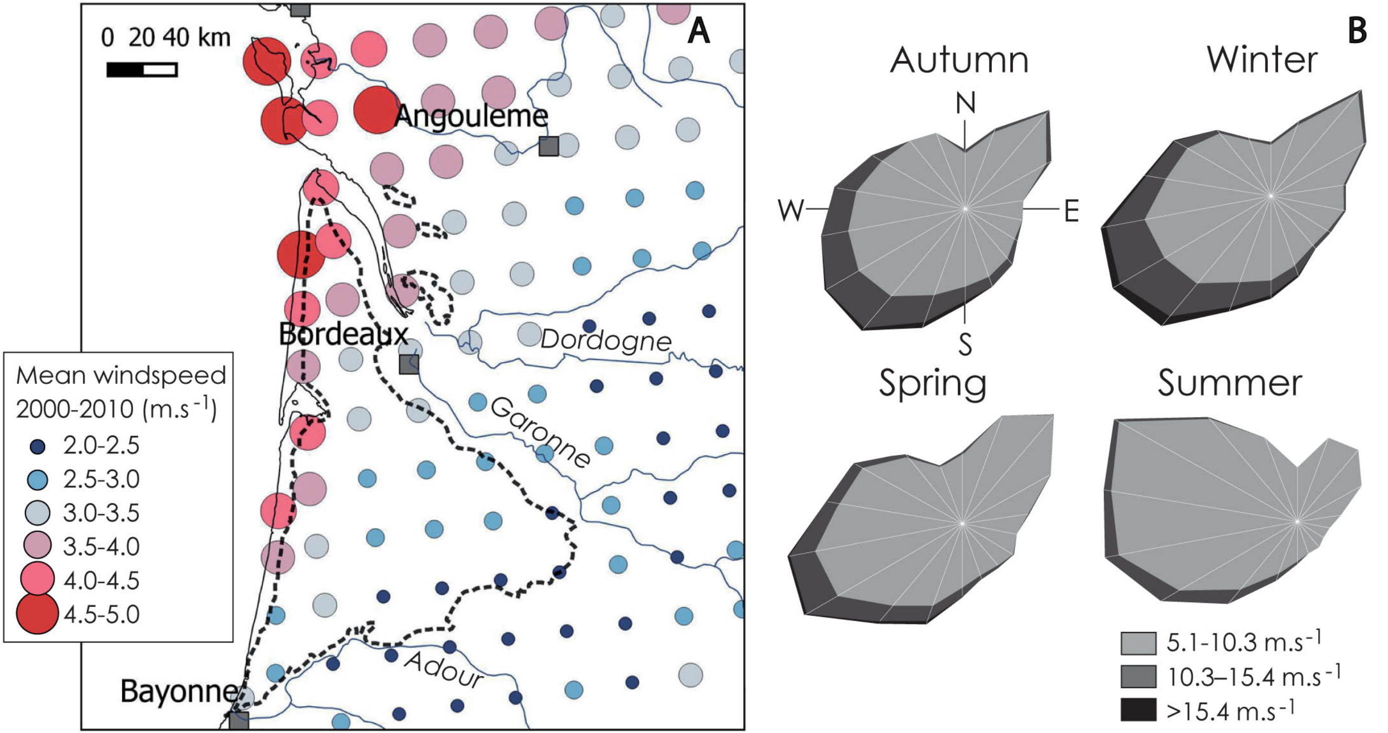

A
0 20 40 km
Angouleme
Bordeaux
Dordogne
Garonne
Adour
Bayonne
Mean windspeed
2000-2010 (m.s-1)
2.0-2.5
2.5-3.0
3.0-3.5
3.5-4.0
4.0-4.5
4.5-5.0
B
Autumn
Winter
Spring
Summer
N
W
E
S
5.1-10.3 m.s-1
10.3–15.4 m.s-1
>15.4 m.s-1

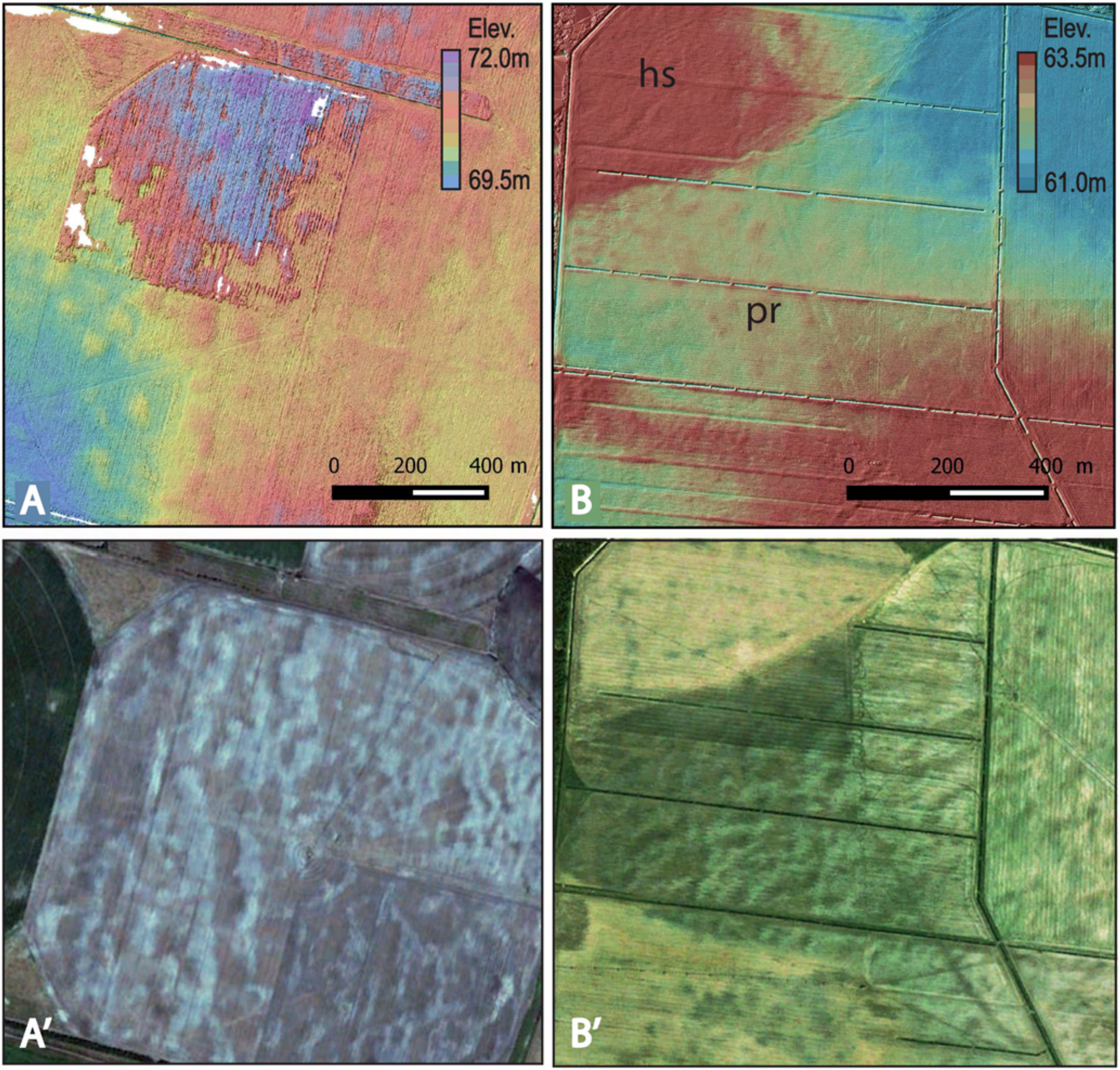
Elev.
72.0m
69.5m
0 200 400 m
A
Elev.
63.5m
61.0m
hs
pr
0 200 400 m
B
A′
B′

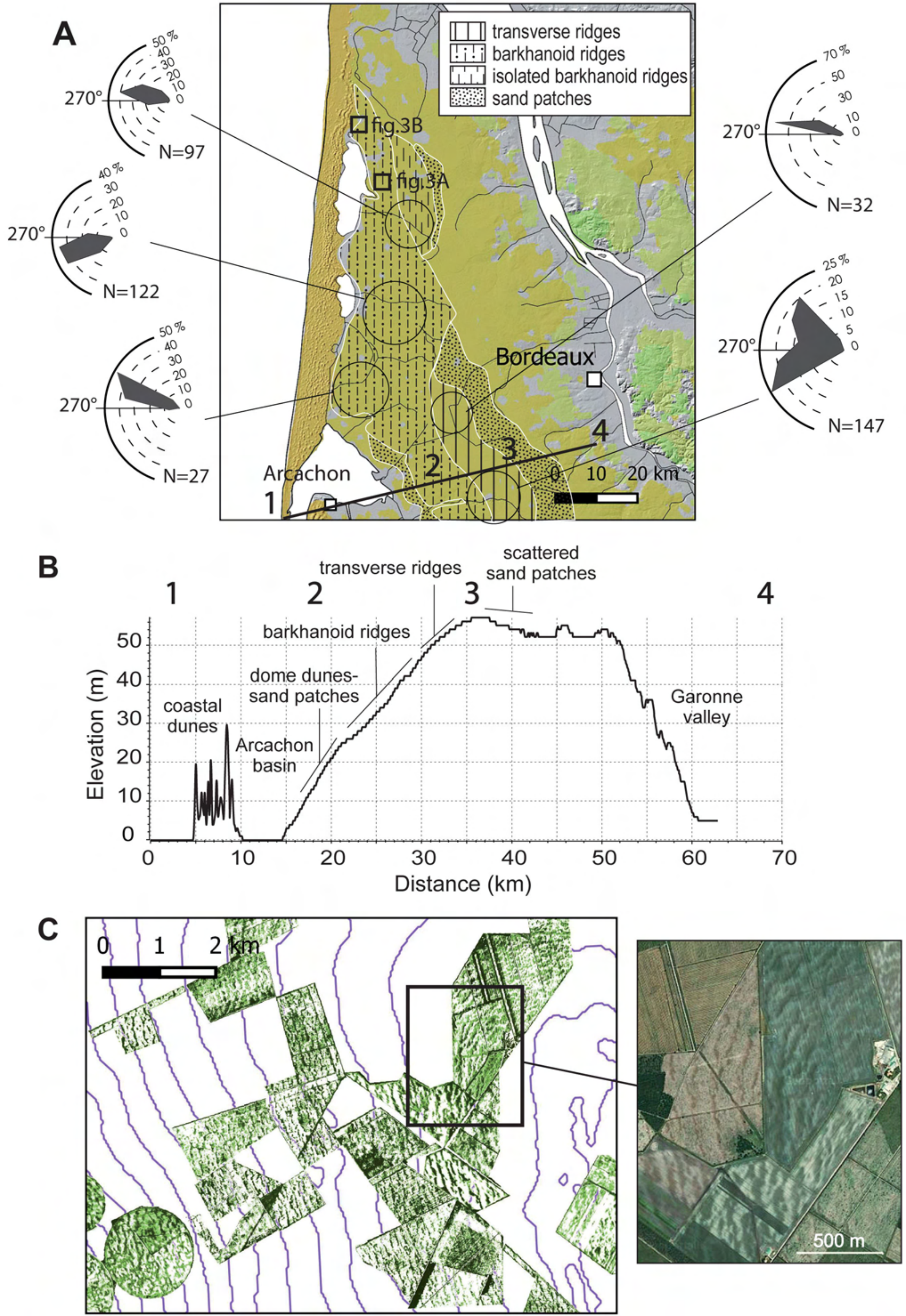
A
transverse ridges
barkhanoid ridges
isolated barkhanoid ridges
sand patches
fig.3B
fig.3A
Bordeaux
Arcachon
1
2
3
4
0 10 20 km
270°
50 % 40 30 20 10 0
N=97
40 % 30 20 10 0
N=122
50 % 40 30 20 10 0
N=27
70 % 50 30 10 0
N=32
25 % 20 15 10 5 0
N=147
B
1 2 3 4
transverse ridges
scattered sand patches
barkhanoid ridges
dome dunes-sand patches
coastal dunes
Arcachon basin
Garonne valley
Elevation (m)
Distance (km)
0 10 20 30 40 50 60 70
C
0 1 2 km
500 m

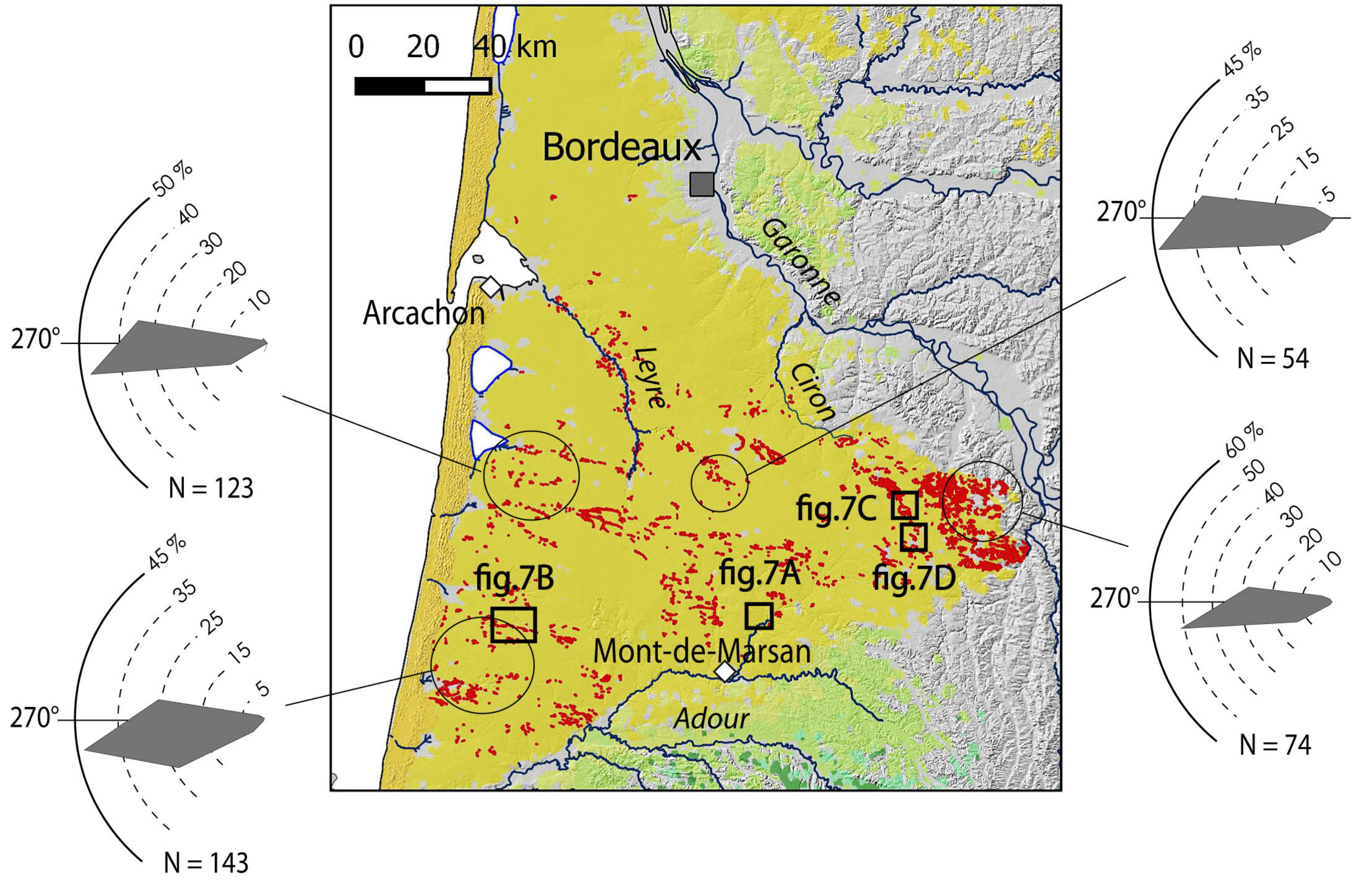
0 20 40 km
Bordeaux
Arcachon
Garonne
Leyre
Ciron
Adour
Mont-de-Marsan
fig.7A
fig.7B
fig.7C
fig.7D
50 %
40
30
20
10
270°
N = 123
45 %
35
25
15
5
270°
N = 143
45 %
35
25
15
5
270°
N = 54
60 %
50
40
30
20
10
270°
N = 74

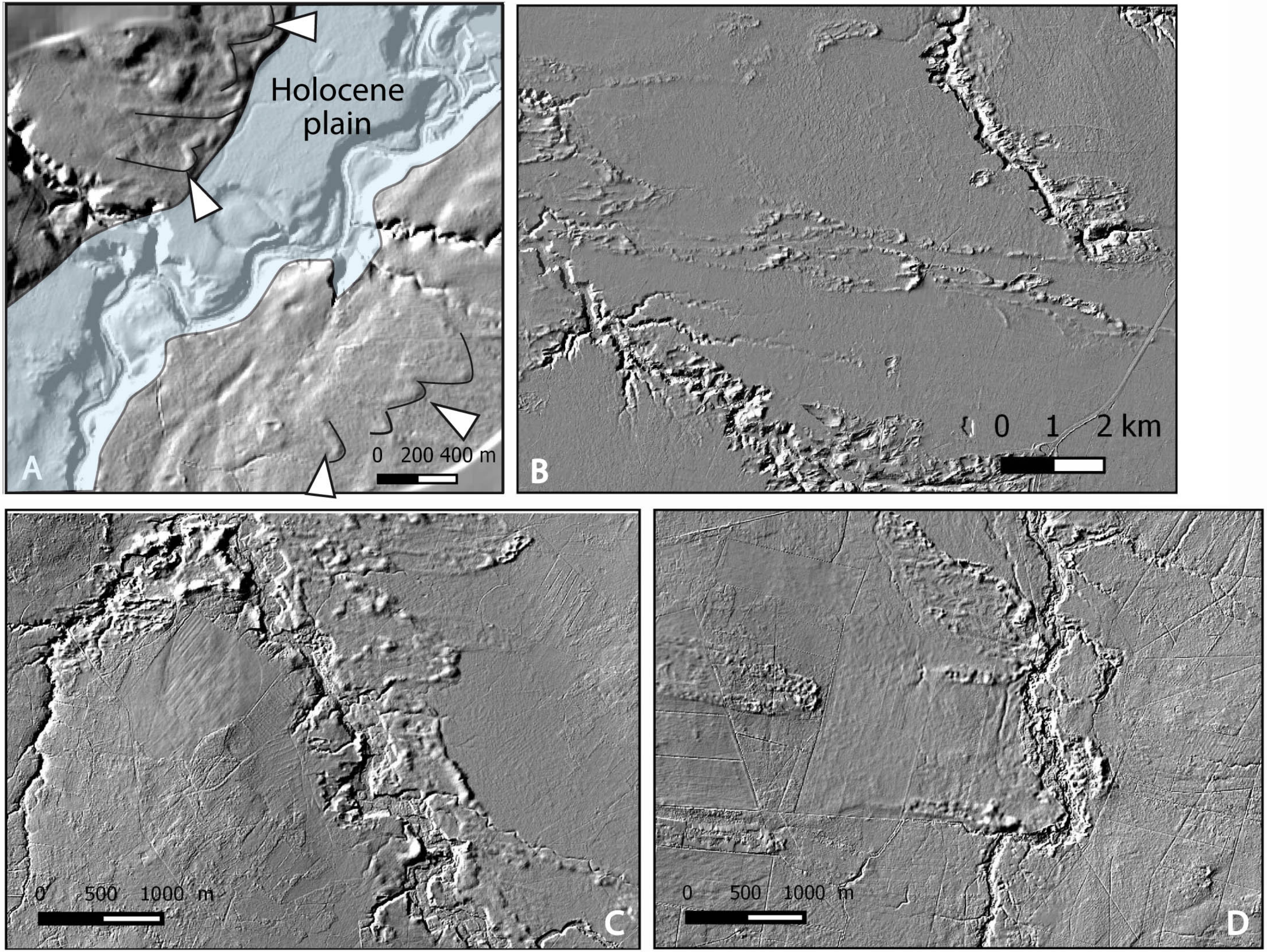
Holocene plain
0 200 400 m
A
0 1 2 km
B
0 500 1000 m
C
0 500 1000 m
D

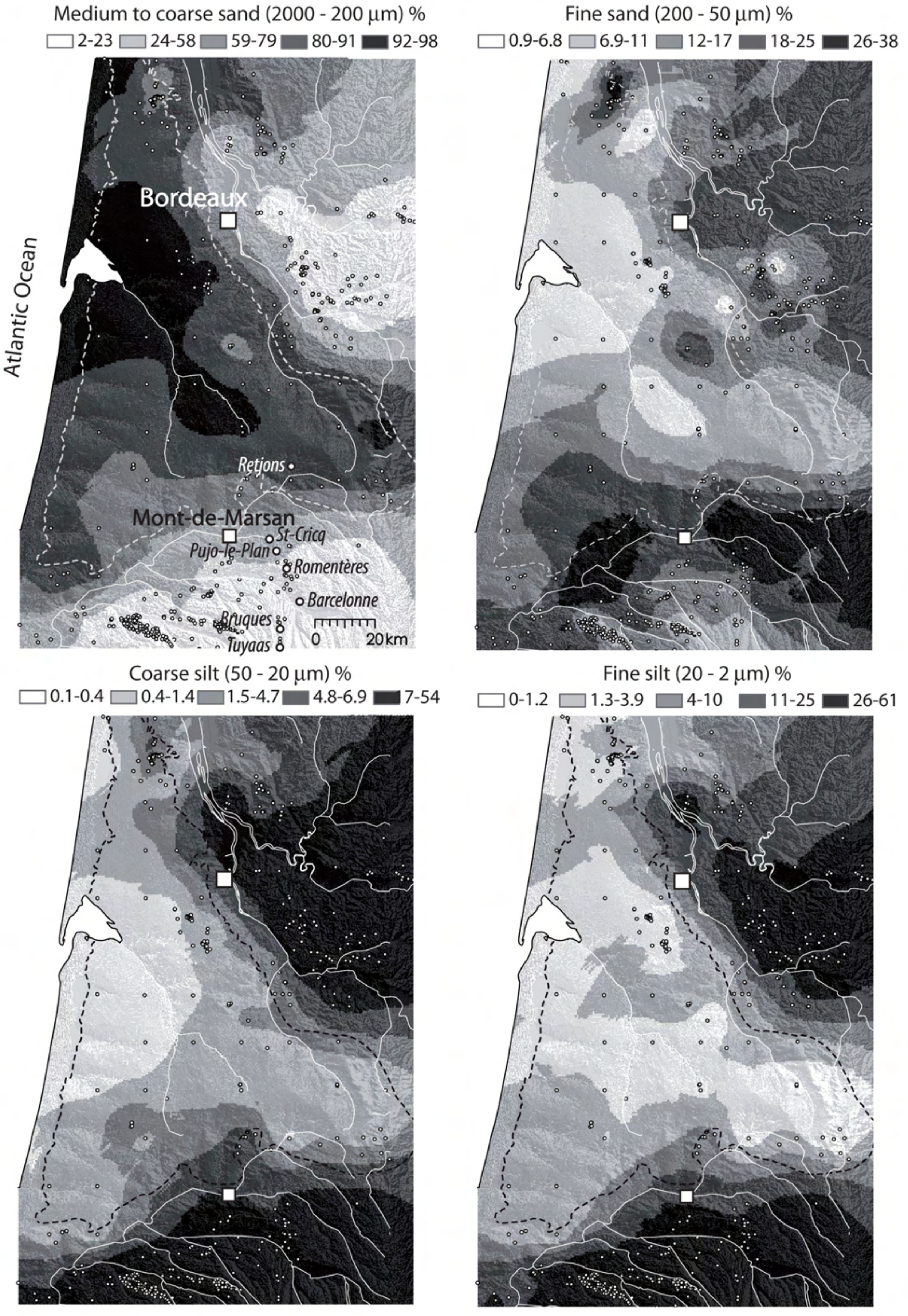
Medium to coarse sand (2000 - 200 µm) %
2-23
24-58
59-79
80-91
92-98
Atlantic Ocean
Bordeaux
Retjons
Mont-de-Marsan
St-Cricq
Pujo-le-Plan
Romentères
Barcelonne
Bruques
Tuyaas
0
20km
Fine sand (200 - 50 µm) %
0.9-6.8
6.9-11
12-17
18-25
26-38
Coarse silt (50 - 20 µm) %
0.1-0.4
0.4-1.4
1.5-4.7
4.8-6.9
7-54
Fine silt (20 - 2 µm) %
0-1.2
1.3-3.9
4-10
11-25
26-61

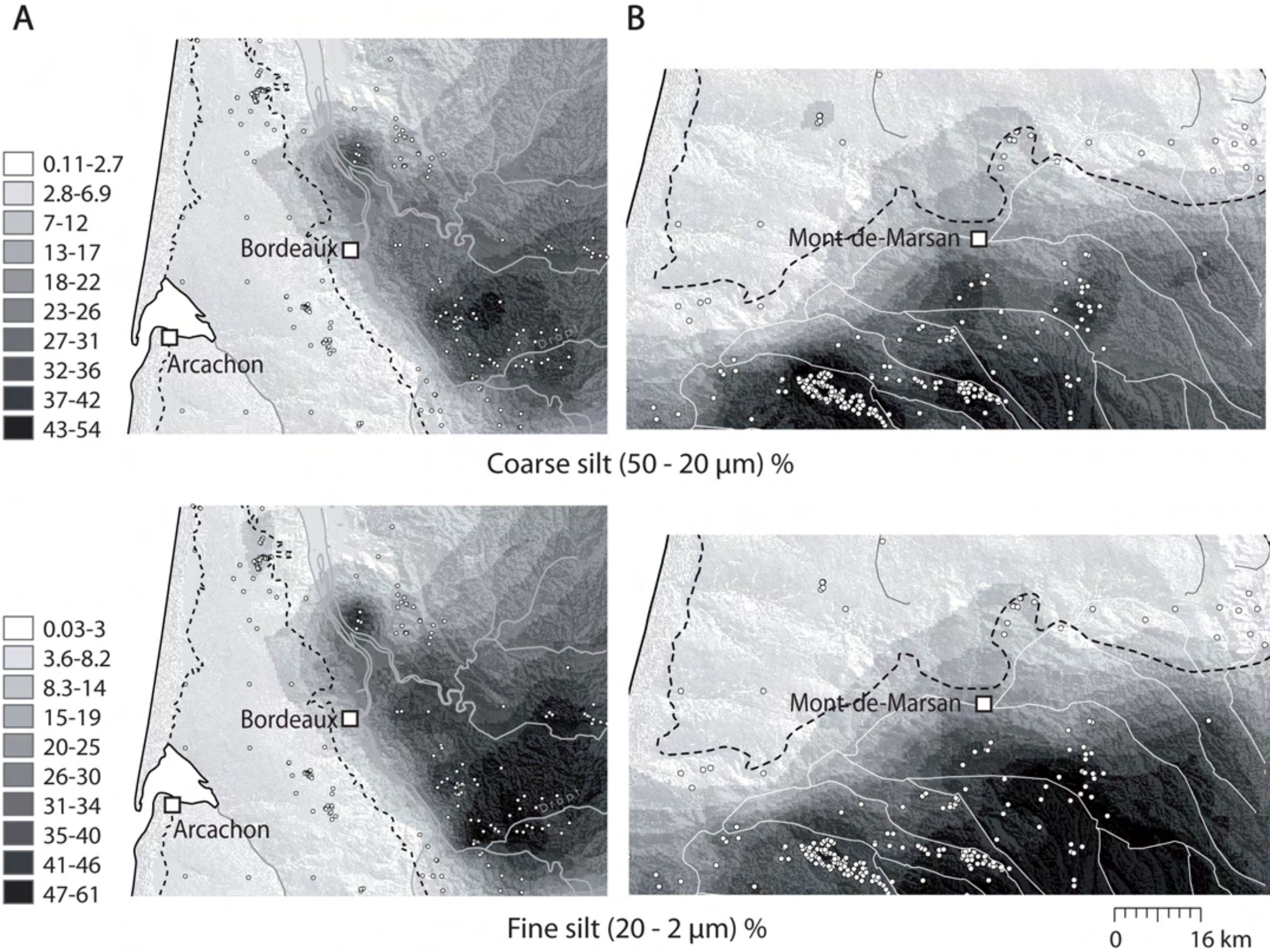
A
B
0.11-2.7
2.8-6.9
7-12
13-17
18-22
23-26
27-31
32-36
37-42
43-54
Bordeaux
Arcachon
Mont-de-Marsan
Coarse silt (50 - 20 µm) %
0.03-3
3.6-8.2
8.3-14
15-19
20-25
26-30
31-34
35-40
41-46
47-61
Bordeaux
Arcachon
Mont-de-Marsan
Fine silt (20 - 2 µm) %
0
16 km

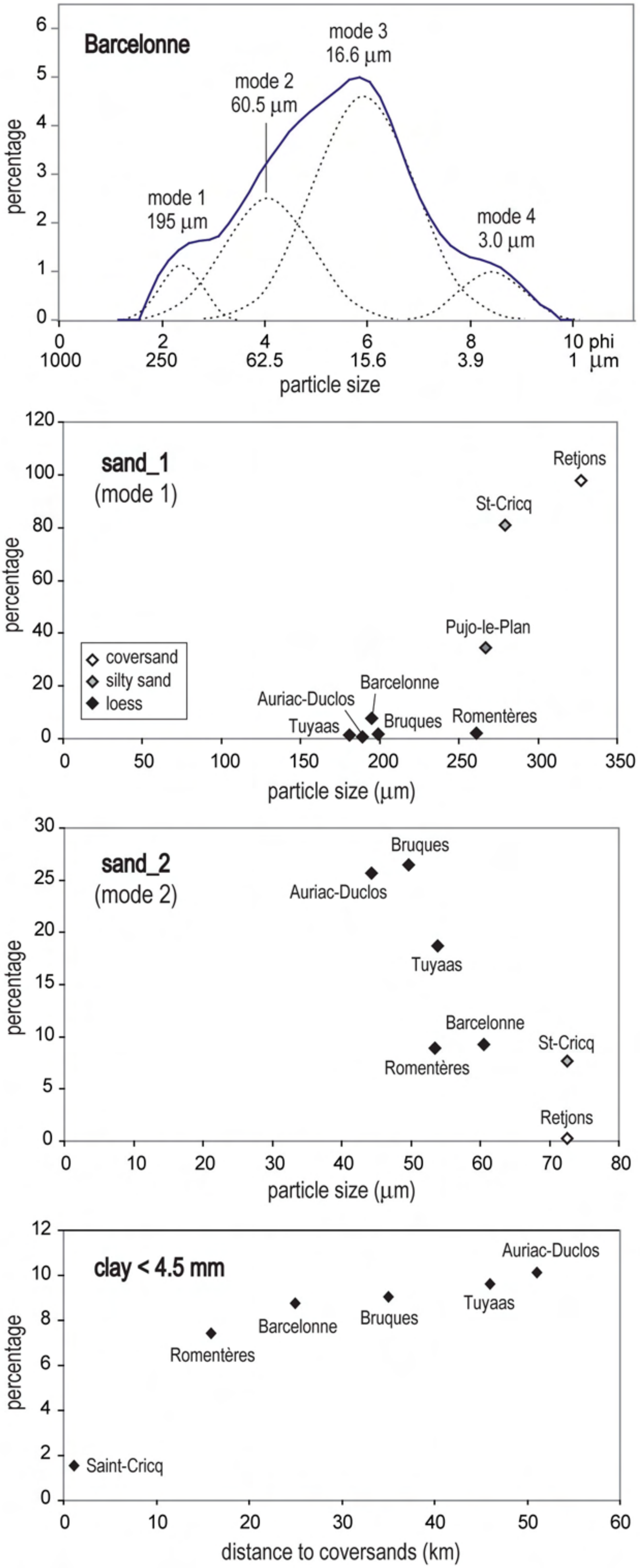
Barcelonne
mode 1
195 µm
mode 2
60.5 µm
mode 3
16.6 µm
mode 4
3.0 µm
percentage
0 1 2 3 4 5 6
0 2 4 6 8 10 phi
1000 250 62.5 15.6 3.9 1 µm
particle size
sand_1
(mode 1)
coversand
silty sand
loess
Retjons
St-Cricq
Pujo-le-Plan
Barcelonne
Auriac-Duclos
Tuyaas
Bruques
Romentères
percentage
0 20 40 60 80 100 120
0 50 100 150 200 250 300 350
particle size (µm)
sand_2
(mode 2)
Bruques
Auriac-Duclos
Tuyaas
Barcelonne
St-Cricq
Romentères
Retjons
percentage
0 5 10 15 20 25 30
0 10 20 30 40 50 60 70 80
particle size (µm)
clay < 4.5 mm
Auriac-Duclos
Tuyaas
Bruques
Barcelonne
Romentères
Saint-Cricq
percentage
0 2 4 6 8 10 12
0 10 20 30 40 50 60
distance to coversands (km)

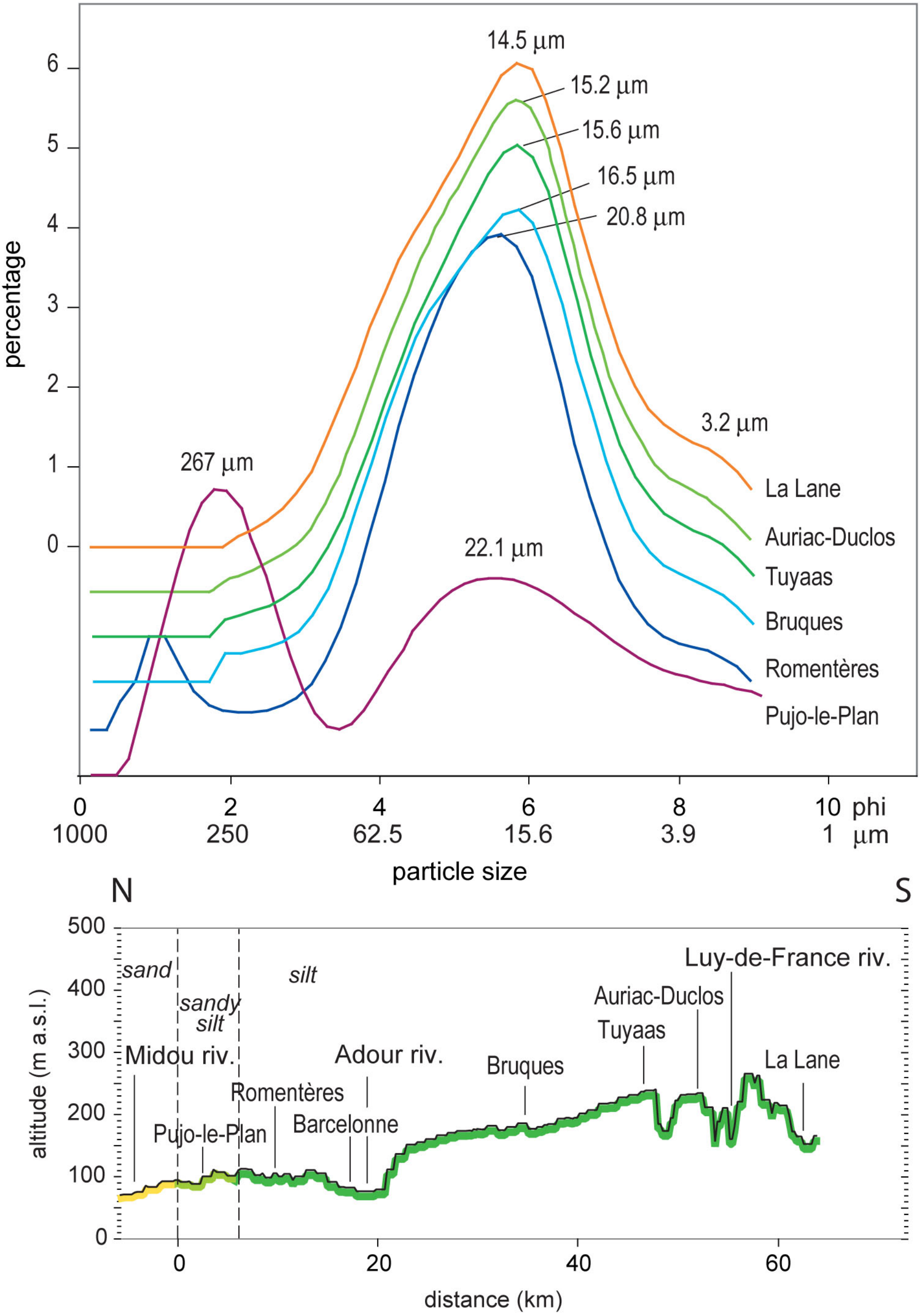
14.5 µm
15.2 µm
15.6 µm
16.5 µm
20.8 µm
267 µm
22.1 µm
3.2 µm
La Lane
Auriac-Duclos
Tuyaas
Bruques
Romentères
Pujo-le-Plan
percentage
0
1
2
3
4
5
6
0 2 4 6 8 10 phi
1000 250 62.5 15.6 3.9 1 µm
particle size
N
S
sand
sandy silt
silt
Midou riv.
Pujo-le-Plan
Romentères
Barcelonne
Adour riv.
Bruques
Tuyaas
Auriac-Duclos
Luy-de-France riv.
La Lane
altitude (m a.s.l.)
0
100
200
300
400
500
0
20
40
60
distance (km)

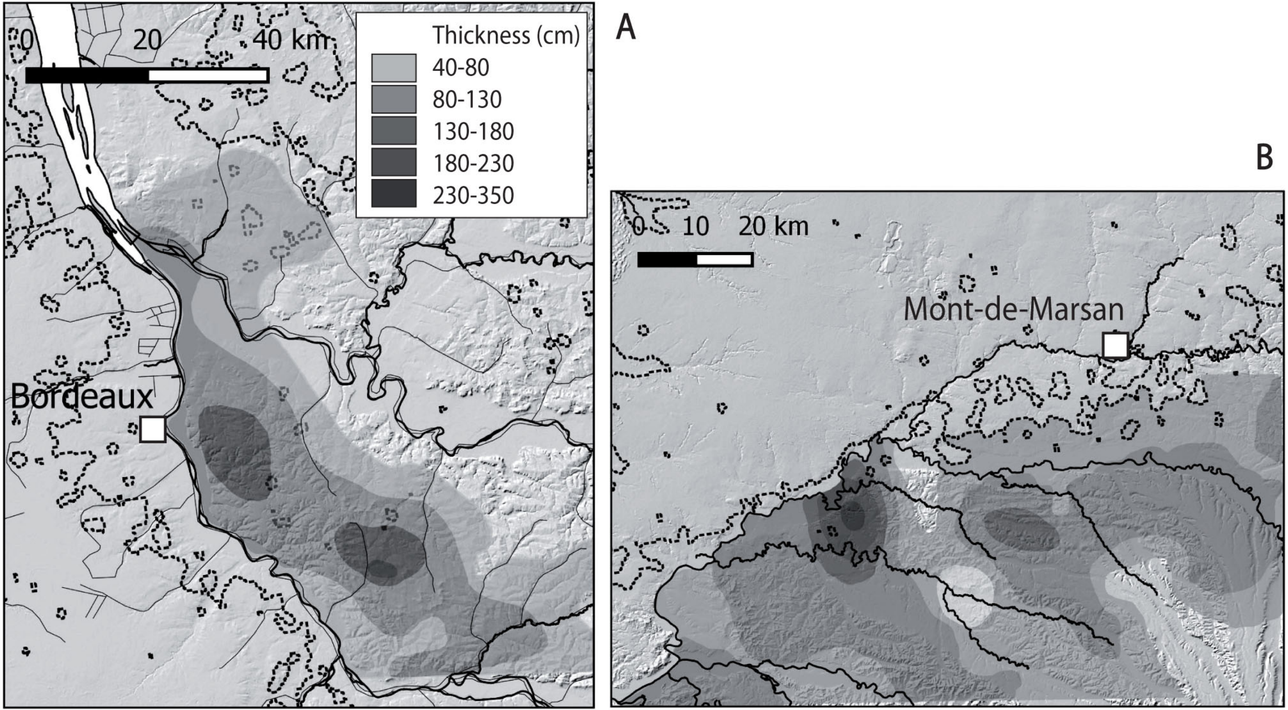
0
20
40 km
Thickness (cm)
40-80
80-130
130-180
180-230
230-350
Bordeaux
A
B
0
10
20 km
Mont-de-Marsan

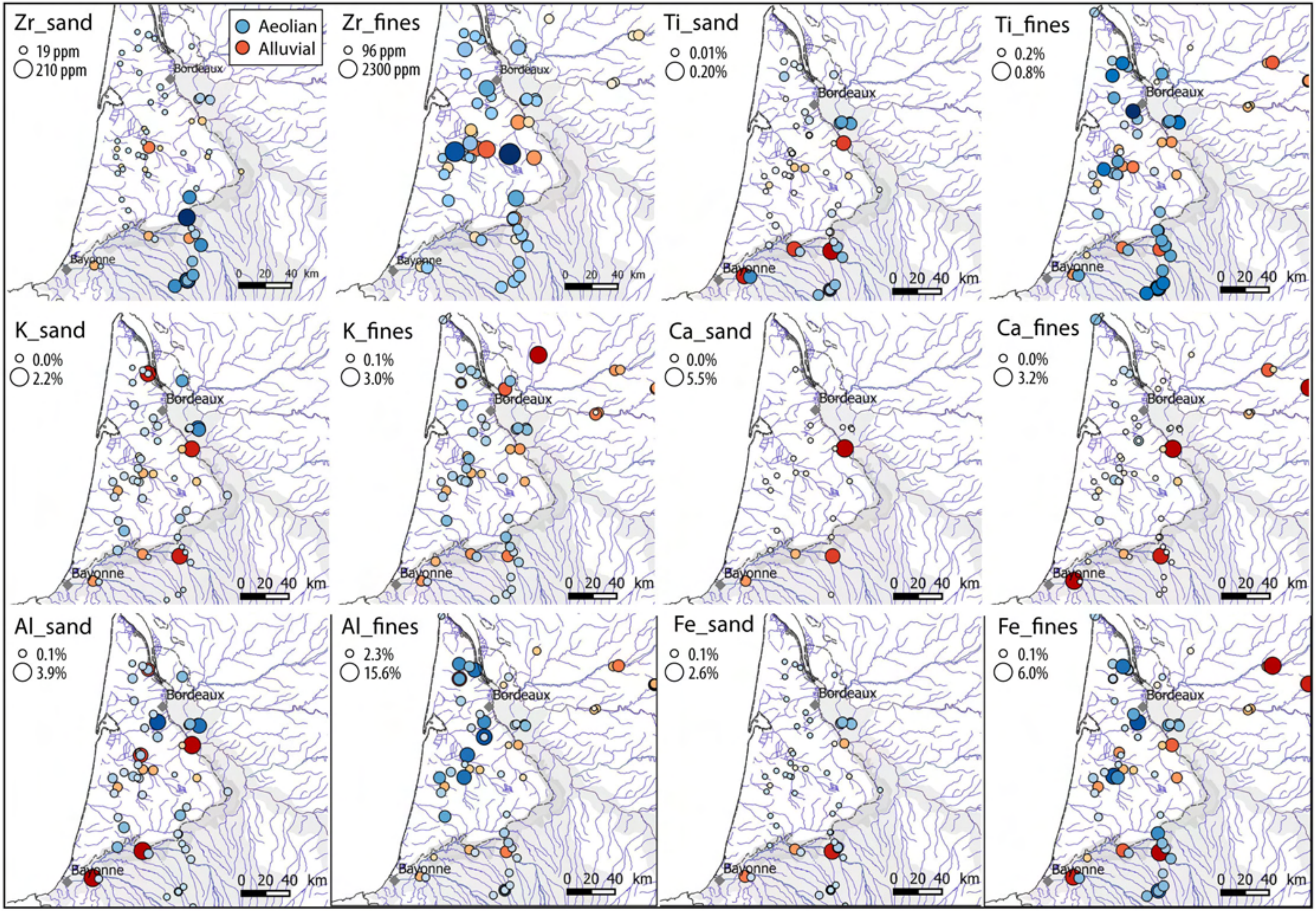
Zr_sand
19 ppm
210 ppm
Aeolian
Alluvial
Zr_fines
96 ppm
2300 ppm
Ti_sand
0.01%
0.20%
Ti_fines
0.2%
0.8%
K_sand
0.0%
2.2%
K_fines
0.1%
3.0%
Ca_sand
0.0%
5.5%
Ca_fines
0.0%
3.2%
Al_sand
0.1%
3.9%
Al_fines
2.3%
15.6%
Fe_sand
0.1%
2.6%
Fe_fines
0.1%
6.0%
Bordeaux
Bayonne
0 20 40 km

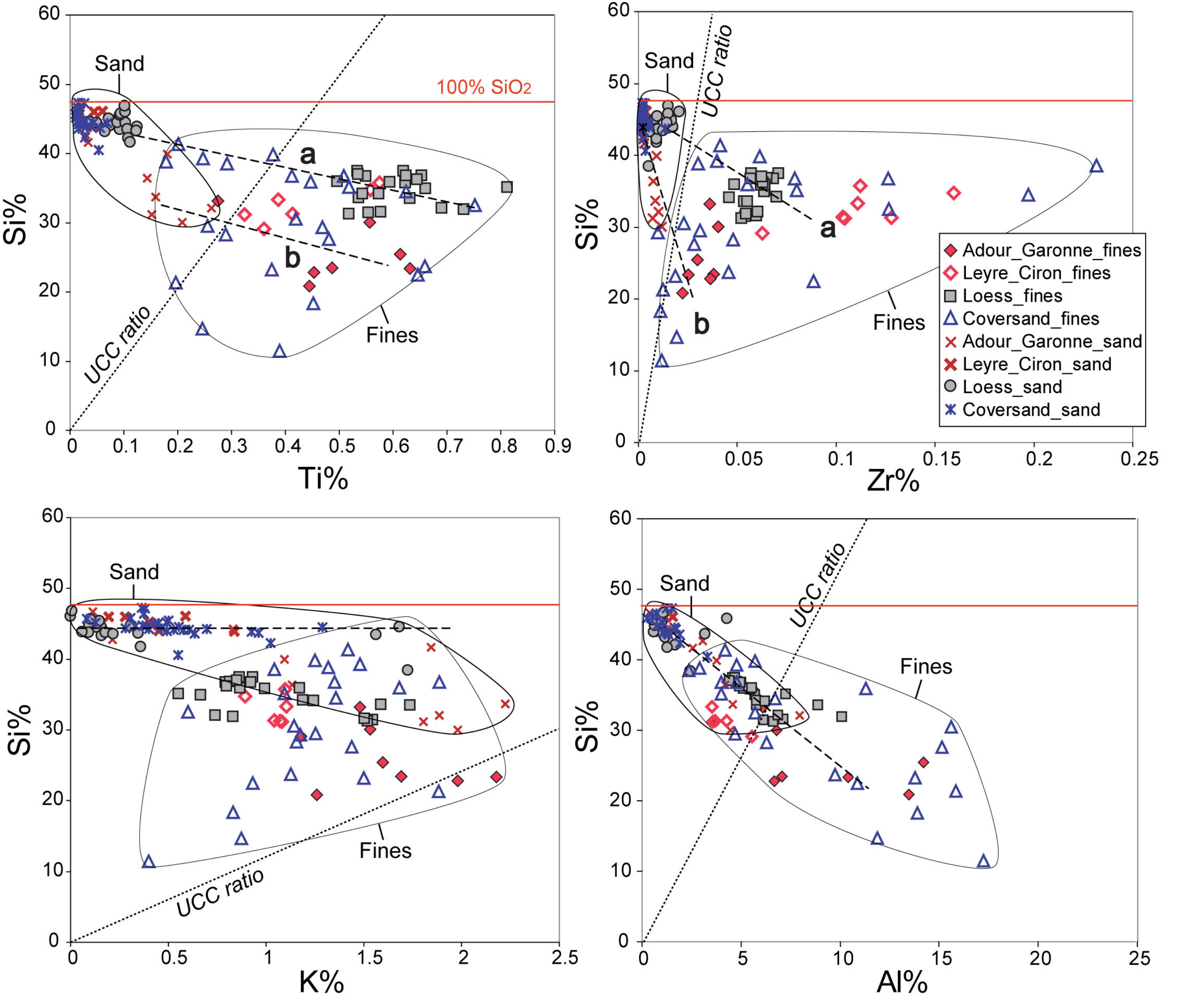

Sand
100% SiO2
a
b
Fines
UCC ratio
Si%
Ti%
Sand
UCC ratio
a
b
Fines
Zr%
Adour_Garonne_fines
Leyre_Ciron_fines
Loess_fines
Coversand_fines
Adour_Garonne_sand
Leyre_Ciron_sand
Loess_sand
Coversand_sand
Sand
Fines
UCC ratio
K%
Sand
UCC ratio
Fines
Al%

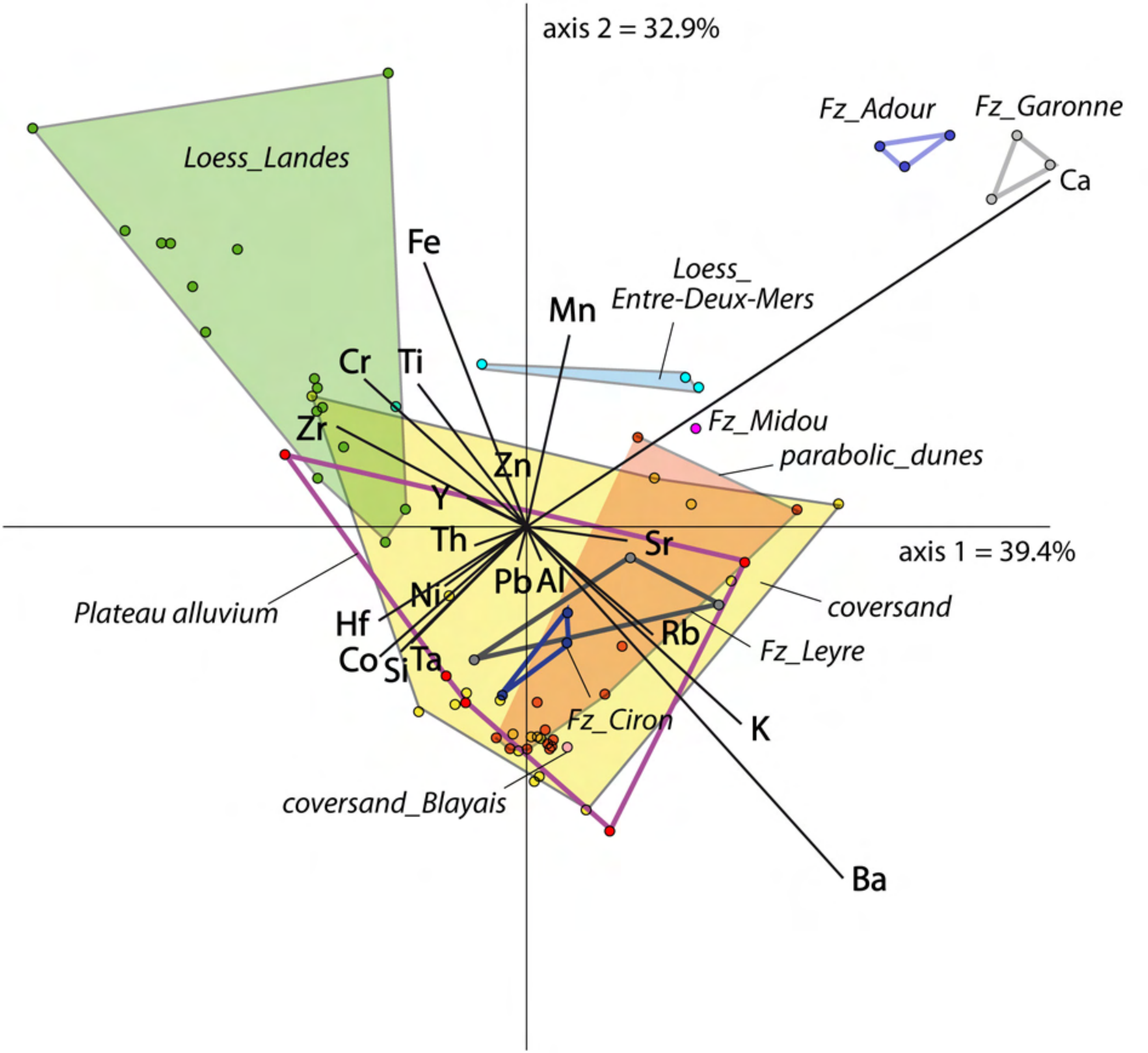
axis 2 = 32.9%
axis 1 = 39.4%
Loess_Landes
Fz_Adour
Fz_Garonne
Ca
Fe
Mn
Loess_
Entre-Deux-Mers
Cr
Ti
Zr
Fz_Midou
parabolic_dunes
Zn
Y
Th
Sr
Pb
Al
Ni
Hf
Co
Si
Ta
Rb
K
Ba
Plateau alluvium
coversand
Fz_Leyre
Fz_Ciron
coversand_Blayais

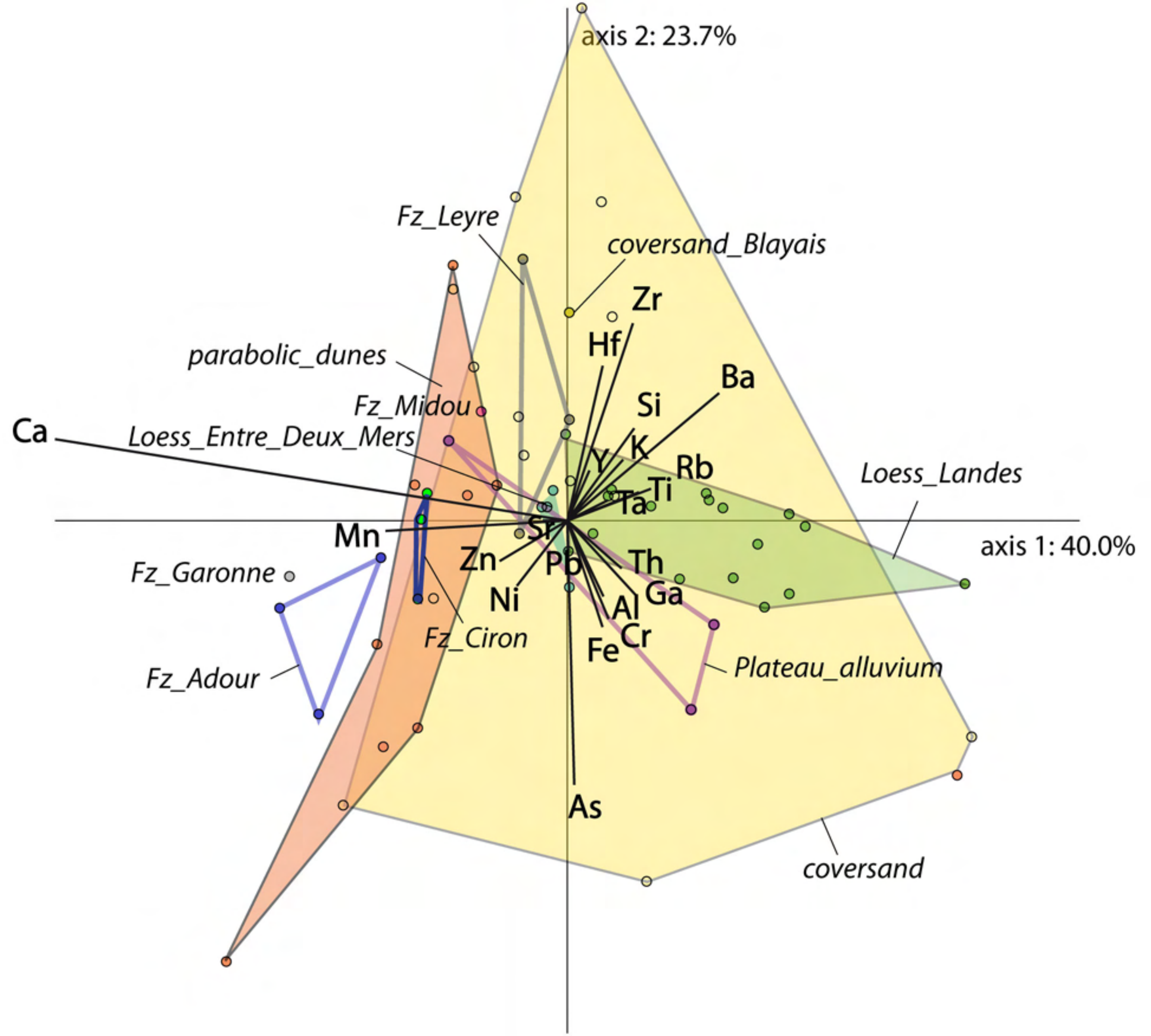
axis 2: 23.7%
axis 1: 40.0%
Fz_Leyre
coversand_Blayais
parabolic_dunes
Fz_Midou
Loess_Entre_Deux_Mers
Loess_Landes
Fz_Garonne
Fz_Adour
Fz_Ciron
Plateau_alluvium
coversand
Ca
Mn
Zr
Hf
Ba
Si
K
Y
Rb
Ti
Ta
Sr
Zn
Pb
Th
Ni
Ga
Al
Cr
Fe
As

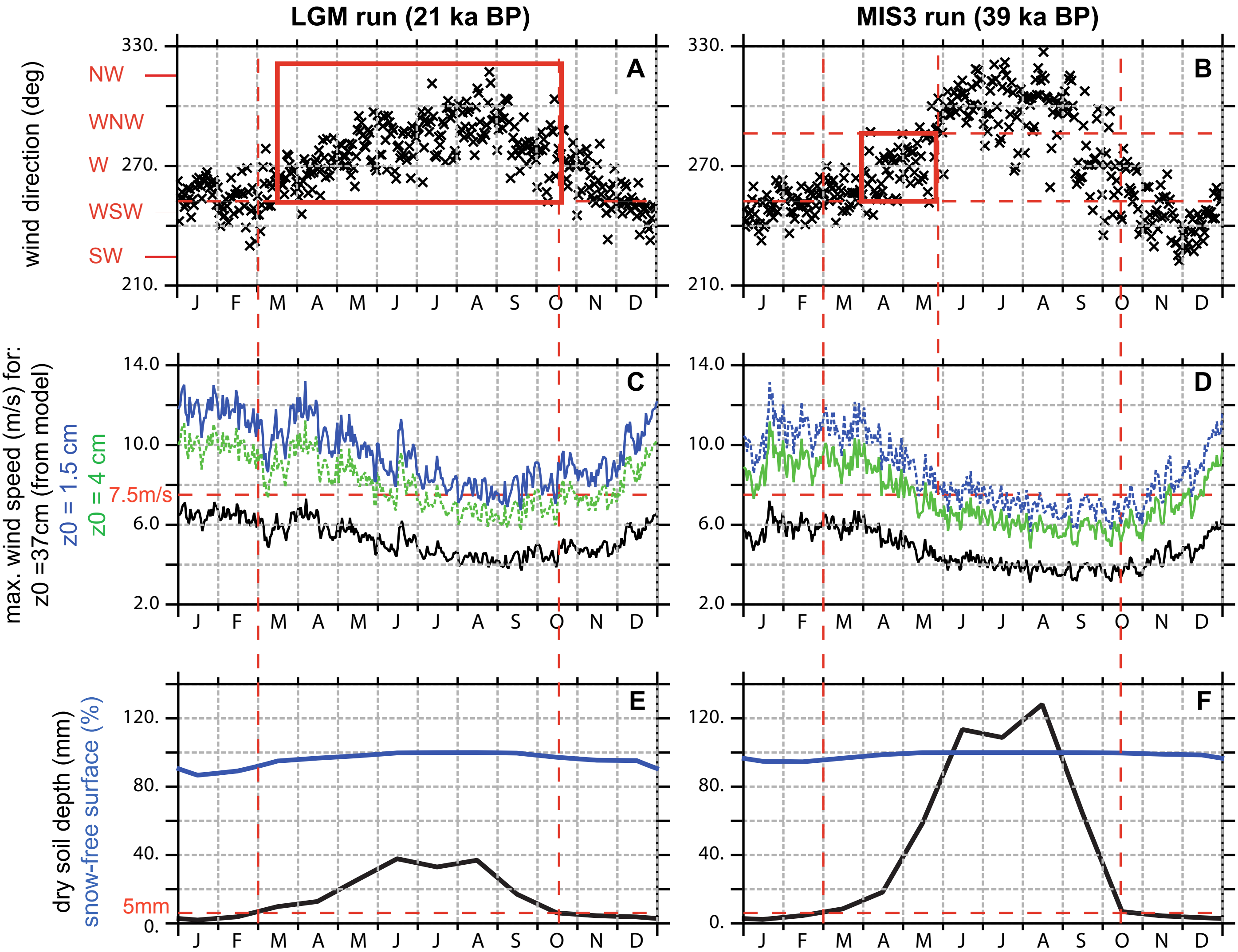
LGM run (21 ka BP)
MIS3 run (39 ka BP)
A
B
C
D
E
F
wind direction (deg)
330.
270.
210.
NW
WNW
W
WSW
SW
max. wind speed (m/s) for:
z0 =37cm (from model)
z0 = 1.5 cm
z0 = 4 cm
14.0
10.0
7.5m/s
6.0
2.0
dry soil depth (mm)
snow-free surface (%)
120.
80.
40.
5mm
0.
J F M A M J J A S O N D